# Effects of crustal assimilation on 238U-230Th disequilibria in continental arc settings

L.B. Kant, K.W.W. Sims, G.M. Yogodzinski, J.M. Garrison, Janne Blichert-Toft, M. Reagan, C.L. Waters, T.P. Mathews, S.R. Scott, P.A. Mothes, et al.

# Effects of crustal assimilation on $^{238}U$-$^{230}Th$ disequilibria in continental arc settings

L.B. Kant[a,b,*], K.W.W. Sims[a,b], G.M. Yogodzinski[c], , J.M. Garrison[d], J. Blichert-Toft[e], M. Reagan[f], C.L. Waters[a,b], T.P. Mathews[a,b], S.R. Scott[a,b], P.A. Mothes[g], M.L. Hall[g], P. Ramon[g], E. Gaunt[g], M. Almeida[g], S. Hidalgo[g]

a) Department of Geology and Geophysics, University of Wyoming, 1000 E. University Avenue, Laramie, Wyoming, 82071, USA

b) Wyoming High Precision Isotope Laboratory, University of Wyoming, 1000 E. University Avenue, Laramie, Wyoming, 82071, USA

c) School of Earth, Ocean, and Environment, University of South Carolina, 701 Sumter St., EWSC617, Columbia, South Carolina 29208, USA

d) Department of Geosciences and Environment, California State University, 5151 State University Drive, Los Angeles, CA 90032-8530

e) Laboratoire de Géologie de Lyon, CNRS UMR 5276, Ecole Normale Supérieure de Lyon, Université de Lyon, 46 Allée d'Italie, 69007 Lyon, France

f) Department of Geoscience, University of Iowa, Iowa City, Iowa, 52242 USA

g) Instituto Geofisico de la Escuela Politecnica Nacional, Ladrón de Guevara E11-253, Facultad de Ingeniería Civil y Ambiental, 6to. Piso, Quito, Ecuador

* Corresponding Author. E-Mail Address: lisa.kant@pnnl.gov (L.B.Kant)

**Abstract**

Compositions of arc magmas depend on several factors and are often thought to reflect conditions in the mantle wedge and at the slab-mantle interface. However, in continental arc settings, magmas are also influenced by assimilation of continental crust. Here, we present measurements and modeling of $^{238}U$-$^{230}Th$ activity ratios, Sr, Nd, Hf, and Pb isotopic compositions, and major and trace element concentrations in young, historic lavas erupted from Reventador, an active stratovolcano in the Ecuadorian Andes. In arc lavas, $^{238}U$-$^{230}Th$ disequilibria are often assumed to reflect processes occurring in the mantle wedge, as U and Th behave differently in this relatively oxidized and fluid-rich environment. Enhanced mobility of hexavalent U in aqueous fluids results in $(^{230}Th/^{238}U) < 1$ and elevated $(^{238}U/^{232}Th)$, which are common in arc lavas. However, the majority of Reventador lavas have $(^{230}Th/^{238}U) = 1.0–1.1$ and $(^{238}U/^{232}Th) = 0.94–1.12$, the latter of which is considerably lower than the depleted mantle ($(^{238}U/^{232}Th) \sim 1.5$, Sims and Hart, 2006). While this Th enrichment could be due to melting of subducted oceanic crust, approximately linear trends between $(^{230}Th/^{232}Th)$, wt. % $SiO_2$, and radiogenic isotope ratios indicate otherwise. We argue that crustal assimilation lowers long-term, or time-integrated, $(^{238}U/^{232}Th)$ in Reventador magmas. To quantify the effects of assimilation we modeled stepwise assimilation and fractional crystallization. Observed trends between $(^{230}Th/^{232}Th)$, $^{87}Sr/^{86}Sr$, $\varepsilon_{Nd}$, $\varepsilon_{Hf}$, and $^{208}Pb/^{206}Pb$ can be reproduced by up to 10% assimilation, which is consistent with previous regional studies. However, reproducing the full spectrum of isotopic diversity among Reventador lavas requires heterogeneous basalt compositions. In a broader context, this study emphasizes the need to consider crustal

processes when examining continental arcs. While $^{238}U$-$^{230}Th$ disequilibria develop in the mantle wedge, they can be overwritten by subsequent interaction with continental crust.

Keywords: Arc Magmatism; Crustal Assimilation; $^{238}U$-series disequilibria

## *1. Introduction*

Uranium-series disequilibria are an important tool for understanding the dynamics of the melting process. Because mantle lithologies beneath ocean basins are relatively simple, U-series measurements in mid-ocean ridge (MORB) and ocean island basalts (OIB) have transformed our understanding of the timescales and mechanisms of melt generation and magma transport (McKenzie, 1985; Spiegelman Elliott, 1993; Lundstrom et al., 1995; Sims et al., 1995, 1999, 2002; Jull et al., 2002; Kokfeldt et al., 2005; Waters et al., 2011; Elkins et al., 2011; Stracke and Bourdon, 2009). In stark contrast, arc magmas have several potential source components, and their compositions record the addition of subducted, altered oceanic crust and sediments to the peridotitic mantle wedge. Additionally, the way materials are transported from the slab to the mantle (i.e., as fluids, melts, or mélange diapirs) significantly affects the resulting magma chemistry (Kessel et al., 2005; Reubi et al., 2014, Yogodzinski et al., 2015).

In arc lavas, positively sloped linear arrays on the ($^{230}Th/^{232}Th$) vs ($^{238}U/^{232}Th$) equiline diagram are often interpreted as isochrons with slopes suggesting that 10-80 Kyr have elapsed since metasomatism (Bourdon et al., 2003; Turner et al., 2003). Many arc lavas, particularly island arcs, have high ($^{238}U/^{232}Th$) and ($^{230}Th/^{238}U$) < 1, or $^{238}U$-excess (see Figure 1 in Reubi et al., 2014). Arc settings are typically oxidizing with relatively high $fO_2$ (Kelley and Cottrell, 2009); in this environment, U is hexavalent and mobile in aqueous

fluids, thereby explaining the observed high ($^{238}U/^{232}Th$) and resulting $^{238}U$-excess which form the positively sloped arrays interpreted as isochrons. However, some arc lavas are characterized by ($^{230}Th/^{238}U$) > 1, or $^{230}Th$-excess. Because of the numerous potential sources and processes involved in arc petrogenesis, $^{230}Th$-excesses in arc magmas are attributed to several possible causes: partial melting, rather than dehydration, of subducted eclogite (Kuritani et al., 2008; Sigmarrson et al., 1998); melting in the garnet lherzolite stability field (George et al., 2003; Thomas et al., 2002); or subducted sediments enriching the mantle in Th (Reubi et al., 2014; Turner and Foden, 2001).

In continental arcs, another complication is interaction between ascending magmas and the overlying crust, as assimilation of thickened and evolved continental crust can modify magma compositions, overprinting metasomatic and deep mantle melting signals (Ankney et al., 2013; Bourdon et al., 2000; Handley et al., 2018; Hora et al., 2009; Huang et al., 2007; Jicha et al., 2007; Jicha et al., 2009; Garrison et al., 2006; Price et al., 2007; Walker et la., 2007; Reubei et al., 2011; 2014). Fortunately, the non-unique interpretation of $^{238}U$-$^{230}Th$ disequilibria in arc magmas, specifically with regards to the cause of $^{230}Th$-excess, can be deconvolved by applying constraints from other geochemical parameters, in particular radiogenic isotopes.

To investigate how interaction between ascending magmas and continental crust impacts $^{238}U$ and $^{232}Th$ abundances and their decay series systematics we measured $^{238}U$-$^{230}Th$ disequilibria, Sr, Nd, Hf, and Pb isotopic compositions, and major and trace element abundances in young lavas from Reventador, an active stratovolcano in the Northern Volcanic Zone of the Andes (NVZ). Reventador Volcano makes an ideal natural laboratory for studying continental arc magma genesis because: 1) it provides a record of young,

known-age lavas, an important requirement for studies utilizing $^{238}$U-series disequilibria; 2) unlike many arc lavas, which often have highly evolved compositions, Reventador is erupting andesitic lavas and can thus provide information on the melting and magma transport processes, without significant magma residence times that will result in U-Th decay toward equilibrium, rendering this system uninterpretable in terms of melting and magma transport processes; and, 3) Reventador is far inland of the arc and has thick crust, providing an opportunity to study the potential effects of assimilation of thickened and evolved continental crust on ascending magmas. As such, these lavas provide a unique and unprecedented opportunity to study crustal assimilation in continental arc lavas and its impact on U-series disequilibria.

## 2 *Geologic Setting*

### 2.1 The Northern Volcanic Zone of the Andes

Reventador is an active volcano in a region referred to the Northern Volcanic Zone (NVZ) of the Andes. The NVZ stretches from 7°N-2°S (Figure 1A). In Colombia, from 7-1°N, the arc consists of a single row of calc-alkaline stratovolcanoes with traits that typify arc lavas including large ion lithophile element (LILE) enrichment and high field strength element (HSFE) depletion (Ancellin et al., 2017 and references therein). In Ecuador, from 1°N-2°S, the arc measures ~150 km from east to west, and at least 50 volcanoes have been active since the Pleistocene (Hall et al., 2008). In the NVZ, the arc is subdivided into four north-south running segments. From west to east these are: 1) the Cordillera Occidental or Western Cordillera; 2) the Inter-Andean Valley, a transpressional basin with scattered volcanic centers; 3) the Cordillera Real or Eastern Cordillera, the locus of Holocene

volcanism; and, 4) the back-arc, where Holocene volcanism is mostly alkalic and characterized by higher FeO/MgO than the other three segments which comprise the main arc (Hall et al., 2008 provides a detailed summary of these subdivisions).

Strontium and Nd isotopic variability between arc segments is well characterized and reflects variable crustal assimilation – both in terms of assimilant composition and amount of crust assimilated (Ancellin et al., 2017; Bryant et al., 2006; Hidalgo et al., 2012). Western Cordillera and Inter-Andean Valley lavas have $^{87}Sr/^{86}Sr$ = 0.7038–0.7044 and $^{143}Nd/^{144}Nd$ = 0.51280–0.51295, or $\varepsilon_{Nd}$ = +2.28 – +5.21. In these arc segments, assimilation of Late Cretaceous-Eocene arc volcanics and accreted oceanic terranes does not shift $^{87}Sr/^{86}Sr$ and $^{143}Nd/^{144}Nd$ because the assimilant and ascending magmas have similar isotopic compositions (Chiaradia, 2009; Jaillard et al., 2009). In contrast, Eastern Cordillera lavas have $^{87}Sr/^{86}Sr$ = 0.7041–0.7047 and $^{143}Nd/^{144}Nd$ = 0.51255–0.51285, or $\varepsilon_{Nd}$ = -2.59 – +3.26. Here, magmas assimilate Paleozoic and Mesozoic metamorphic and intrusive rocks with evolved isotopic compositions (Ancellin et al., 2017, and references therein; Hammersley et al., 2022). Back-arc lavas have $^{87}Sr/^{86}Sr$ and $\varepsilon_{Nd}$ values similar to Western Cordillera and Inter-Andean Valley lavas due to minimal crustal assimilation by ascending lavas (Garrison et al., 2018).

Lead isotope variability likely also reflects variable crustal assimilation. Throughout the main arc, $^{206}Pb/^{204}Pb$ = 18.8–19.1. However, Eastern Cordillera lavas have $^{207}Pb/^{204}Pb$ = 15.6–15.7 and $^{208}Pb/^{204}Pb$ = 38.6–39.0, whereas Western Cordillera lavas exhibit approximately constant $^{207}Pb/^{204}Pb$ = 15.6 and $^{208}Pb/^{204}Pb$ = 38.5–39.8, and Inter-Andean Valley lavas fall into both groups. These results are also consistent with assimilation of Paleozoic-Mesozoic metamorphic and intrusive basement in the east and

Cretaceous-Eocene accreted terranes and arc rocks in the west (Ancellin et al., 2017; Chiaradia et al, 2004). In back-arc and Eastern Cordillera volcanoes, including Reventador, Pb isotopes define a third trend with $^{206}Pb/^{204}Pb < 18.9$, $^{207}Pb/^{204}Pb \sim 15.6$, and $^{208}Pb/^{204}Pb < 38.8$ (Ancellin et al., 2017). This trend requires a spatially restricted, non-radiogenic Pb source such as mid-upper crustal Jurassic intrusions emplaced in the Sub-Andean zone (Ancellin et al., 2017; Chiaradia et al., 2004; this study). This distinct Pb isotopic signature could also be due to displacement of crustal blocks with non-radiogenic Pb along the Cosanga Fault, part of the NE-SW running Chingual-Cosanga-Pallatanga-Puna shear zone (CCPP; Figure 1A) (Baize et al., 2020).

The Carnegie Ridge, a 250-km-wide, 14-19 km thick aseismic ridge, subducts roughly perpendicular to the trench between 0° and 2°S. This feature formed between 12 and 20 Ma during plume-ridge interaction between the Galapagos Plume and Spreading Center (Figure 1A; Sallarès and Charvis, 2003). Although several studies examined the influence of the Carnegie Ridge on magmatism in the NVZ, its effects are debated. One area of disagreement is whether subduction of young crust leads to slab melting. The primary support for this argument is geochemical; lavas with adakitic trace element compositions, such as elevated Sr/Y and light/heavy rare earth element (LREE/HREE) ratios, are ubiquitous in Ecuador, yet absent north of the ridge in Colombia (Ancellin et al., 2017; E. Bourdon et al., 2003; Defant and Drummond, 1990; Hidalgo et al., 2012; Narvaez et al., 2018). Some authors also suggest that the onset of adakitic magmatism and ridge subduction were roughly coincident (E. Bourdon et al., 2003; Gutscher et al., 2000; Samaniego et al., 2005). However, estimates of the onset of ridge subduction vary from < 1-15 Ma, while adakite-like magmatism began between 0.1 and 1.6 Ma (Michaud et al.,

2009, and references within). Furthermore, thermal modeling predicts that subducting crust dehydrates prior to crossing the wet basalt solidus, even in cases where the slab crust is relatively young (Syracuse et al., 2010). To address this discrepancy, others propose that the slab is flat or shallowly dipping, in which case the pressure-temperature path of the slab would briefly intersect the wet basalt solidus and melt (Gutscher et al., 2000). Historically, a lack of recorded Benioff-Wadati zone seismicity made it difficult to accurately characterize slab dip beneath the arc and verify this hypothesis (Syracuse and Abers, 2006). However, recent seismological studies with local networks suggest that the slab dips 25-35° (Yepes et al., 2016). Consequently, adakite-like trace element compositions may be unrelated to the Carnegie Ridge. Instead, these traits could result from assimilation of garnet-bearing lower crust (Chiaradia et al., 2011, 2020; Garrison et al., 2006; Michaud et al., 2009), or stabilization of residual garnet during mantle melting, and subsequent fractional crystallization of clinopyroxene, garnet, and amphibole in the lower crust (Bryant et al., 2006; Bloch et al., 2017).

Alternatively, adakite-like trace element compositions may result from melting along the Grijalva Fracture Zone (GFZ), an abandoned rift formed during Miocene break-up of the Farallon plate that enters the trench near 2.5°S (Figure 1A). The GFZ juxtaposes oceanic crust of different ages, with older Farallon crust to the SE and younger Carnegie Ridge crust to the NW (Yepes et al., 2016). This age difference (> 9 Myr) results in a density contrast across the GFZ, which in turn could lead to flexing and tearing of the slab. Mantle flow through this tear could cause melting along slab edges, generating the adakitic traits that are prevalent in the NVZ (Narvaez et al., 2018; Rosenbaum et al., 2018; Yepes et al., 2016; Yogodzinski et al., 2001).

## 2.2 Reventador Volcano

Reventador Volcano is located ~90 km northeast of Quito, Ecuador, in the eastern foothills of the Andes, or the Sub-Andean Zone (Figure 1A). Although it is located in between the main and back-arcs, we classify it as part of the main arc, since many of its geochemical traits are more similar to main-arc volcanoes than back-arc volcanoes (see Section 4.1). Reventador consists of an older horseshoe-shaped caldera which surrounds an extinct cone and the currently active cone. Prior to the onset of activity in 2002, the altitude of the active cone was 3560 m, a height of > 1500 m above the lowest part of the caldera floor (2000 m), and slightly higher than the western rim of the caldera (Hall et al., 2004).

El Reventador translates to "The Exploder" and has a historical record of eruptive activity dating back to the 16$^{th}$ century. Because of its remote location and heavy precipitation in the area surrounding the volcano, direct observation was historically difficult. However, between 1541 and 2002 there were at least 29 eruptive phases. Periods of eruptive activity during the 20$^{th}$ century occurred in 1898-1912, 1926-1929, 1944, 1958-1960, 1972, 1973, 1974, and 1976, producing pyroclastic flows, lava flows, lahars, and mm-sized ash fall deposits in the Inter-Andean Valley. The current phase of activity began in November of 2002, when the initial VEI-4 eruption produced a Plinian column that eventually reached a height of 16-17 km, resulting in closure of the international airport in Quito and deposition of up to 5 mm of ash in the Inter-Andean Valley (Hall et al., 2004). Activity has continued intermittently to the present (Almeida et al. 2019).

Previous geochemical studies of Reventador focused on the shallow plumbing system of the volcano and conditions in the magma chamber immediately preceding

eruption (Ridolfi et al., 2008, Samaniego et al., 2008). Both studies reported textural evidence for mixing, such as reverse zoning, resorption, and overgrowth. Additionally, they observed that Reventador lavas contain phases such as olivine and orthopyroxene which are not in equilibrium with andesitic magma. Both authors suggested that injection of basaltic magma into a shallow andesitic magma chamber triggered eruption, consistent with the occurrence of volcano-tectonic seismicity with focal depths of 10-11 km prior to the 2002-2005 eruptions (Hall et al., 2004).

## *3. Materials and Methods*

Twenty whole-rock volcanic samples of known age were analyzed: three erupted during the 20$^{th}$ century, four erupted in 2016, and 13 erupted between 2002 and 2010 (Figure 1B). Twentieth century and 2002-2010 samples were collected during expeditions in 2008 and 2010. Samples from 2016 were collected inside the crater during aerial surveys that same year. Isotopic compositions of three basement samples collected south of Reventador were also analyzed; two hornblende biotite granodiorites (SU-11 and SU-112), and one biotite schist containing trace < 1 mm garnet and pyrite (REV-130). Location data is given in supplementary Table S1. $^{87}Sr/^{86}Sr$ and $^{143}Nd/^{144}Nd$ isotope ratios of granodiorite SU-11 were previously published by Garrison et al. (2018). Major and trace elements were analyzed by X-ray fluorescence and inductively coupled plasma mass spectrometry (ICPMS) at Washington State University, USA, according to procedures outlined in Jarvis (1988) and Johnson et al. (1999). Strontium, Nd, Hf, Pb, and $^{238}U$-series isotopic analyses of all samples were performed at University of Wyoming (UWYO), USA, using a ThermoFisher NEPTUNE PLUS multi-collector inductively coupled plasma

mass spectrometer (MC-ICPMS). Additional Hf and Nd isotopic analyses were performed at the Ecole Normale Supérieure in Lyon (ENSL), France; and additional Hf isotopic analyses were conducted at University of South Carolina (USC), USA. However, since the ENSL and USC data sets do not include all samples analyzed in this study, they are not included in the main text. The supplementary text contains a comparison of all three data sets, and a description of the analytical procedures followed at ENSL and USC.

### 3.1 Sr, Nd, Hf and Pb isotope analysis

Approximately one gram of sample powder was digested in Savillex beakers using a mixture of concentrated trace metal grade $HNO_3$, HF, and $HClO_4$. After complete digestion, samples were redissolved and stored in 3N HCl and trace (< 1%) $HBO_3$ at a concentration of 10 mg rock/ml solution. For each sample, four separate fractions were aliquoted from the main solution accordingly: 1) approximately 5 ml for Sr, Nd, and Pb isotopic compositions; 2) approximately 5 ml for Hf isotopic composition; 3) approximately 1 ml for U and Th isotope dilution; and 4) approximately 1-2 ml for U and Th isotopic compositions.

Strontium, rare earth element (REE), and Pb fractions were separated from the whole rock solution using Bio-Rad AG50W-X8 (200-400 mesh) cation-exchange resin in HCl. The Sr fraction was further purified using Sr-specific ion-exchanger Sr-Spec resin (Eichrom Technologies), while Nd was separated from the other REE with the REE-specific ion-exchanger Ln-Spec resin (Eichrom Technologies). Lead was purified with Bio-Rad AG1-X8 (100-200 mesh) anion-exchange resin (Hart et al., 2004; Hart and Blusztajn, 2006; Sims et al., 2008a; 2013a). Hafnium was collected from a separate aliquot and

isolated from the whole rock solution using Ln-Spec resin (Münker et al., 2001). Prior to isotope analysis, the purified Sr, Nd, and Hf fractions were dried down and then redissolved in a 1N $HNO_3$ + trace HF solution. Samples were introduced into the plasma using either the standard sample introduction system (a quartz dual cyclonic double pass spray chamber) or an ESI Apex IR desolvating nebulizer to improve sensitivity for low-concentration samples. Measurements were conducted in static mode using Faraday collectors. Results were corrected for instrumental mass bias relative to $^{88}Sr/^{86}Sr$ = 8.375209, $^{146}Nd/^{144}Nd$ = 0.7219, and $^{179}Hf/^{177}Hf$ = 0.7325 and then normalized relative to the daily averages of NBS987 ($^{87}Sr/^{86}Sr$ = 0.71024), JNdi-1 ($^{143}Nd/^{144}Nd$ = 0.51207), and Merck1 ($^{176}Hf/^{177}Hf$ = 0.282155). Prior to analysis, the Pb fractions were dried down, redissolved in a 1N $HNO_3$ + trace HF solution and spiked with Tl standard NBS997. Lead isotope compositions were corrected for instrumental mass bias relative to NBS/SRM 997 $^{203}Tl/^{205}Tl$ = 0.41891 (White et al., 2000). Compositions were further normalized to the daily average of Pb standard NBS981. NBS981 values from Thirwall (2002) ($^{206}Pb/^{204}Pb$ = 16.9417, $^{207}Pb/^{204}Pb$ = 15.4996, and $^{208}Pb/^{204}Pb$ = 36.7240) were used so that results were consistent with previous results produced at UWYO.

Internal run precisions (2σ SE) for $^{87}Sr/^{86}Sr$ and $^{143}Nd/^{144}Nd$ were ≤ 16 ppm, while those for $^{176}Hf/^{177}Hf$ were ≤ 32 ppm, and $^{206}Pb/^{204}Pb$, $^{207}Pb/^{204}Pb$, and $^{208}Pb/^{204}Pb$ were ≤ 94 ppm. USGS reference materials AGV-2 and BCR-1 were analyzed for quality assurance (Table 1). Our long-term mean and external reproducibility (2σ) plus literature values for these standards are listed in supplementary text 2. Total procedural blanks were ≤ 450 pg for Sr, ≤ 120 pg for Nd, ≤ 190 pg for Hf, and ≤ 160 pg for Pb. In all cases, the blank/sample ratio was ≤ 2 ‰ and did not affect results (average voltages of the most abundant isotopes

were 1-10 V for Nd, Hf, and Pb, and 10-20 V for Sr). The insignificance of the procedural blanks on the data is demonstrated by the reproducibility of our reference material measurements, both internally and when compared with other laboratories (Supplementary Text).

### 3.2 $^{238}$U-series isotope analysis

Uranium and Th concentrations and isotope ratios were measured following procedures outlined in Lane and Sims (2000); Sims et al. (2008b, 2013b), Ball et al. (2008), and Scott et al. (2019). Concentrations were measured using isotope dilution. Each aliquot was spiked with $^{233}$U and $^{229}$Th. Uranium and Th were separated from the sample matrix using Bio-Rad AG1-X8 (100-200 mesh) anion-exchange resin in $HNO_3$ and analyzed together on Faraday detectors. The resulting $^{238}U/^{233}U$ and $^{232}Th/^{229}Th$ measurements were corrected for mass bias by sample-standard bracketing with U010 using $^{235}U/^{238}U$ = 0.01014 (Richter and Goldberg, 2003). A separate aliquot was prepared for isotope ratio measurements. Uranium and Th were separated from the sample matrix with Bio-Rad AG1-X8 (200-400 mesh) anion-exchange resin in $HNO_3$, and then separated from each other with Bio-Rad AG1-X8 (200-400 mesh) anion-exchange resin in HCl. Measurements were conducted using the axial secondary electron multiplier (SEM) and retarding potential quadrupole (RPQ) in addition to the Faraday detectors. For ($^{234}U/^{238}U$), $^{234}$U was measured with the SEM/RPQ, while $^{238}$U was measured on a Faraday collector. Measurements were corrected for mass bias by sample-standard bracketing with U010, assuming $^{234}U/^{238}U=5.4483\times10^{-5}$ (Richter and Goldberg, 2003). For $^{230}Th/^{232}Th$, $^{230}$Th was measured on the SEM/RPQ and $^{232}$Th was measured on a Faraday collector. An exponential tail

correction was used to remove $^{232}Th$ tailing counts on $^{230}Th$. Measurements were corrected for mass bias by sample-standard bracketing with IRMM-035, using $^{230}Th/^{232}Th = 1.13810^{-5}$ (Sims et al., 2008b).

Uncertainties for U and Th concentrations (2σ) range from 1.1–1.6 and 1.1–1.3%, respectively, and are dominated by the uncertainties in the spike concentrations, which are 1.4 and 1.2%, respectively. Procedural blanks were < 1000 pg for both U and Th, which is well within the 2σ uncertainty. Internal run precisions (2σ SE) for ($^{234}U/^{238}U$) and ($^{230}Th/^{232}Th$) are 0.05-0.15% and 1.05-1.15%, respectively. Analyses of USGS standards BCR-1 and RGM-2 agree, within the uncertainties, with the recommended values from Scott et al. (2019) (Table 2).

## 4. *Results*

### 4.1 Major and trace elements

Reventador lavas range from basaltic andesite to andesite (52.38–59.41 wt. % $SiO_2$) and are calc-alkaline with medium $K_2O$, plotting near the medium-high $K_2O$ dividing line (Figure 2). Samples are characterized by traits that typify arc magmas, such as HFSE depletion and LILE enrichment. They also are LREE enriched, which is common throughout the NVZ (Figures 3 and 4; Ancellin et al., 2017; Bryant et al., 2006; Hidalgo et al., 2012). LREE/HREE and light/middle REE (LREE/MREE) increase with increasing wt. % $SiO_2$ (Figure 4; complete major and trace element data are listed in Supplementary Table S1).

Major and trace element concentrations of Reventador lavas vary depending on the age of the sample. For instance, samples erupted in 2016 are among the most evolved,

having wt. % $SiO_2$ = 57.02–58.07. Additionally, while 20$^{th}$ century samples span the entire range of wt. % $SiO_2$, they have lower levels of LREE/HREE enrichment compared to younger samples (Figure 4A and B).

**4.2 Sr, Nd, Hf, and Pb isotopes**

Reventador lavas have $^{87}Sr/^{86}Sr$ = 0.704420–0.704589, $\varepsilon_{Nd}$ = +1.68 – +2.81, $\varepsilon_{Hf}$ = +3.81 – +5.46, $^{206}Pb/^{204}Pb$ = 18.576–18.640, $^{207}Pb/^{204}Pb$ = 15.607–15.612, and $^{208}Pb/^{204}Pb$ = 38.482–38.525 (Table 2). $^{208}Pb/^{206}Pb$ = 2.067–2.072 in Reventador lavas are the highest measured in the NVZ. The Hf isotope data are the first published for the NVZ. In comparison to other volcanoes in the NVZ, Reventador lavas have relatively high $^{87}Sr/^{86}Sr$ and low $\varepsilon_{Nd}$, with values similar to those observed at Eastern Cordillera volcanoes, but distinct from back-arc volcanoes such as Sumaco (Figure 5; Ancellin et al., and references therein; Hammersley et al., 2022; Garrison et al., 2018). Excluding $^{207}Pb/^{204}Pb$, the isotopic data form approximately linear trends in Sr-Nd-Pb-Hf isotope space (Figure 6). There are also systematic trends between isotope ratios and wt. % $SiO_2$ (Figure 7) as well as LREE/HREE such as La/Yb, as well as weaker trends between isotope ratios and LREE/MREE such as La/Sm (Figure 8).

**4.3 U-Th disequilibria**

In Reventador lavas, ($^{238}U/^{232}Th$) = 0.929–1.181 and ($^{230}Th/^{232}Th$) = 0.979–1.118. Most samples have $^{230}Th$-excesses or are within error of equilibrium, with ($^{230}Th/^{238}U$) = 0.989–1.131 (Figure 9; Table 2). Four samples have $^{238}U$-excesses outside of error with equilibrium, ($^{230}Th/^{238}U$) = 0.867–0.969. Since all samples erupted in the 20$^{th}$ and 21$^{st}$

centuries, these values are equivalent to the activity ratios at eruption. $^{238}$U-series disequilibria have been measured at two other volcanoes in the NVZ, Cotopaxi and Nevado del Ruiz (Garrison et al., 2006; Schaeffer et al., 1994). Although lavas from these volcanoes and Reventador have similar ($^{230}$Th/$^{238}$U), Reventador lavas extend to lower ($^{238}$U/$^{232}$Th) (Figure 9).

($^{230}$Th/$^{232}$Th) is positively correlated with $\varepsilon_{Nd}$, $\varepsilon_{Hf}$, $^{208}$Pb/$^{204}$Pb, and $^{206}$Pb/$^{204}$Pb; negatively correlated with $^{87}$Sr/$^{86}$Sr, $^{208}$Pb/$^{206}$Pb, La/Yb, and wt. % $SiO_2$; and weakly correlated with La/Sm (Figure 10). Although samples with $^{238}$U-excesses and samples with $^{230}$Th-excesses have overlapping ranges of wt. % $SiO_2$, samples with $^{238}$U-excesses are generally more evolved with higher wt. % $SiO_2$, La/Sm and Pb/Ce (Figure 11). However, there are no systematic differences in $^{87}$Sr/$^{86}$Sr, $\varepsilon_{Nd}$, $\varepsilon_{Hf}$, $^{208}$Pb/$^{206}$Pb, and La/Yb between samples with $^{238}$U-excesses and samples with $^{230}$Th-excesses.

**4.4 Basement samples**

We also analyzed three basement samples that were collected 50-70 km SW of Reventador (Tables 1 and 2). These samples have $^{206}$Pb/$^{204}$Pb = 18.043–18.456, $^{208}$Pb/$^{204}$Pb = 37.841–38.264, and $^{208}$Pb/$^{206}$Pb = 2.073–2.098 (Figure 5), which are consistent with previous measurements of the Sub-Andean basement (Chiaradia et al., 2004). $^{87}$Sr/$^{86}$Sr, $\varepsilon_{Nd}$, and $\varepsilon_{Hf}$ range from 0.7044–0.7057, -0.6 – +3.6, and +0.47 – +15.27, respectively. Although $^{87}$Sr/$^{86}$Sr and $\varepsilon_{Nd}$ values reported here are within the range observed in previous studies, $^{87}$Sr/$^{86}$Sr measurements are relatively low while $\varepsilon_{Nd}$ is relatively high compared to previously reported values for Eastern Cordillera basement samples (Hammersley et al., 2022). Additionally, the ranges in $^{87}$Sr/$^{86}$Sr and $\varepsilon_{Nd}$ suggest that the Sub-Andean basement

is heterogeneous, containing some isotopically primitive rocks, which are compositionally similar to the Western Cordillera basement, in addition to more evolved rocks. ($^{238}U/^{232}Th$) is also highly variable, ranging from 0.6025–1.3142, but < 1 in the more evolved samples, SU-11 and SU-112.

## 5 *Discussion*

### 5.1 Reventador is a main-arc volcano

Because of its location east of the Eastern Cordillera, some previous studies have classified Reventador as a back-arc volcano (e.g., Garrison et al., 2018). However, we prefer to include Reventador in the main arc, as Reventador lavas are calc-alkaline like main-arc volcanoes, whereas back-arc lavas are characterized by higher FeO/MgO (Figure 2A). However, in some respects Reventador lavas are also distinct from main-arc lavas. For instance, Reventador lavas are more mafic than other main-arc lavas, which are typically andesitic to dacitic. Reventador lavas also have higher trace element concentrations than other main-arc andesites and basaltic andesites (Figures 2 and 3). Nonetheless, these differences are overshadowed by the differences between Reventador lavas and NVZ back-arc lavas, which have even lower wt. % $SiO_2$ (39–60), are typically alkaline, and have higher trace element concentrations (Figure 3). Consequently, we classify Reventador as part of the main arc, and posit that the melting regime beneath Reventador is more akin to that of the Eastern Cordillera volcanoes than that of back-arc volcanoes such as Sumaco (Garrison et al., 2018).

### 5.1 Crustal assimilation controls isotopic variability and LREE/HREE

Previous studies of isotopic diversity in the NVZ suggest that relatively high $^{87}Sr/^{86}Sr$ and low $\varepsilon_{Nd}$ in the Eastern Cordillera result from assimilation of geochemically mature continental crust, which is absent in the Western Cordillera and Inter-Andean Valley (Ancellin et al., 2017; Bryant et al., 2006; Hidalgo et al., 2012). Therefore, the linear trends in Sr-Nd-Hf-Pb isotope space observed in Reventador lavas most likely reflect crustal assimilation, and systematic variability between isotopic ratios and wt. % $SiO_2$ indicates that this process plays a pivotal role in magma evolution (Figures 6 and 7). In addition, among samples erupted since 2002, LREE/HREE ratios (i.e., La/Yb) are positively correlated with wt.% $SiO_2$, $^{87}Sr/^{86}Sr$, and $^{208}Pb/^{206}Pb$, while negatively correlated with $\varepsilon_{Nd}$ and $\varepsilon_{Hf}$, suggesting that crustal assimilation produces adakite-like trace element ratios (Figures 4 and 8). This finding is consistent with previous studies proposing that adakite-like characteristics in the NVZ originate in the lower crust (e.g., Garrison et al., 2006), rather than in the subducting plate or mantle wedge. However, this relationship is not seen in 20$^{th}$ century samples, which are characterized by La/Yb < 20 (Figures 4 and 8).

**5.3 Processes changing the melts initial U/Th ratio and its impact on ($^{230}Th/^{238}U$)**

Time-dependent melting processes can change ($^{230}Th/^{232}Th$) (McKenzie, 1985; Spiegelman and Elliott, 1993, Lundstrom et al., 1995; Sims et al., 1999). However, in the case of Reventador lavas we argue that this effect is small relative to other petrological influences. Therefore, we use the lavas' ($^{230}Th/^{232}Th$) as a proxy for the ($^{238}U/^{232}Th$) of their spatially and temporally integrated source. Since U is more mobile than Th under typical subduction zone conditions (e.g., Kessel et al., 2005), arc lavas are often characterized by $^{238}U$-excesses. Over time, $^{238}U$-excess leads to high ($^{230}Th/^{232}Th$) due to

409 ingrowth of $^{230}$Th (Reubi et al., 2014; Turner et al., 2003). Low ($^{230}$Th/$^{232}$Th) measured in
410 Reventador lavas ($\leq$ 1.12) requires addition of Th to the mantle wedge and/or a source with
411 low ($^{238}$U/$^{232}$Th). In some arcs, Th is added to the mantle wedge via sediment melts and/or
412 fluids, which lowers ($^{238}$U/$^{232}$Th) and eventually ($^{230}$Th/$^{232}$Th) (Turner and Foden, 2001;
413 DuFrane et al., 2009; Reubi et al., 2014). However, Colombian Margin sediments have
414 high ($^{238}$U/$^{232}$Th) equal to 7.469 (Plank, 2014). Therefore, in the NVZ subducted sediment
415 is likely to raise the U/Th of the mantle wedge, regardless of how U and Th are fractionated
416 during melting or dehydration.

417 Whether the subducted crust melts in the NVZ is a matter of debate (E. Bourdon et
418 al., 2003; Garrison et al., 2006; Hidalgo et al., 2012; Michaud et al., 2009; see Section 2.1).
419 However, the effects of slab melting on U-series disequilibria should be considered as Th is
420 more mobile than U at higher temperatures, especially in the presence of residual garnet,
421 and therefore addition of melts or supercritical fluids to the mantle wedge may result in
422 $^{230}$Th-excess (Sigmarrson et al., 1998; Kessel et al., 2005; Kuritani et al., 2008). Eastern
423 Galapagos Spreading Center basalts (EGSC), with average ($^{238}$U/$^{232}$Th) = 0.947, can be
424 used to approximate ($^{238}$U/$^{232}$Th) of Carnegie Ridge basalts (Kokfeldt et al., 2005). Small
425 degree partial melting of the EGSC (5-10%) at 1000°C and 4 GPa results in ($^{238}$U/$^{232}$Th) =
426 0.623–0.707 and initial ($^{230}$Th/$^{238}$U) = 1.34–1.52 (Kessel et al., 2005). Addition of 0.25–1%
427 of these melts to the depleted mantle, with ($^{238}$U/$^{232}$Th) and ($^{230}$Th/$^{232}$Th) = 1.52 (Sims and
428 Hart, 2006), generates ($^{230}$Th/$^{232}$Th) =1.049–1.267 and ($^{238}$U/$^{232}$Th) = 0.782–1.160. Because
429 ($^{230}$Th/$^{232}$Th) will decrease due to decay of $^{230}$Th, the ($^{230}$Th/$^{232}$Th) of this mixture will
430 eventually encompass the values measured in Reventador lavas (Figure 12). However,
431 seafloor alteration raises ($^{238}$U/$^{232}$Th) of the oceanic crust (Kelley et al., 2005). Therefore,

mixtures of depleted mantle and EGSC melts are likely to have higher ($^{238}U/^{232}Th$) than shown in Figure 12; over time this will result in higher ($^{230}Th/^{232}Th$). Consequently, in this case the effect of melting subducted crust on $^{238}U$-$^{230}Th$ disequilibria is unclear.

Instead, we suggest that low ($^{230}Th/^{232}Th$) among Reventador lavas reflects crustal assimilation. This argument is supported by trends among ($^{230}Th/^{232}Th$), $^{87}Sr/^{86}Sr$, $\varepsilon_{Nd}$, $\varepsilon_{Hf}$, and $^{208}Pb/^{206}Pb$, which extend towards measured isotopic compositions of Sub-Andean basement samples (Figure 10). It is also consistent with conclusions from previous studies demonstrating that assimilation can lower ($^{238}U/^{232}Th$) and produce $^{230}Th$-excesses (Ankney et al., 2013; Bourdon et al., 2000; Handley et al., 2018; Hora et al., 2009; Huang et al., 2007; Jicha et al., 2007; Jicha et al., 2009; Garrison et al., 2006; Price et al., 2007; Walker et al., 2007). In particular, $^{230}Th$-excess among Cotopaxi andesites has been attributed to partial melting of the garnet-bearing lower crust (Garrison et al., 2006).

### 5.4 Modeling the evolution of Reventador Lavas

Evolution of continental arc lavas, such as those of Reventador, can be thought of as a multi-step process. Broadly, and for modeling purposes, these processes can be grouped into two steps: first, magma generation in the mantle wedge; followed by magma ascent through and interaction with the continental crust. Unfortunately, processes occurring at the slab-mantle interface and in the mantle-wedge are not well understood in the NVZ, and are thus difficult to quantify. Therefore, we use parental basalt compositions estimated from previous studies, and focus instead on processes occurring in the crust which overprint parental basalt compositions.

### 5.4.1 The finite-difference assimilation-fractional crystallization model

We use a finite-difference assimilation-fractional crystallization model (FD-AFC; DePaolo, 1981; 1985) to quantify the effects of assimilation on $^{87}Sr/^{86}Sr$, $\varepsilon_{Nd}$, $\varepsilon_{Hf}$, $^{208}Pb/^{206}Pb$, ($^{230}Th/^{232}Th$), ($^{238}U/^{232}Th$), La/Yb, and La/Sm.

The model parameters and equations are defined as follows:

$M$ = mass of magma in magma chamber

$\bar{m}_c = \frac{dM_c}{dt}$, where $M_c$ is the mass of crystallized material ($\overline{m}_c \neq 0$)

$\bar{m}_a = \frac{dM_a}{dt}$, where $M_a$ is the mass of assimilated material

$C_m, C_o, C_a$ = concentration of an element in the magma at time $t_n$, the initial magma, and the assimilant, respectively

$\varepsilon_m, \varepsilon_o, \varepsilon_a$ = isotopic ratio in the magma at time $t_n$, the initial magma, and the assimilant, respectively

$D$ = the bulk solid/liquid partition coefficient, $D > 0$

To simplify, we let $\bar{a} = \frac{\bar{m}_a}{\bar{m}_c}$, so that $\frac{dM_a}{dt} = \bar{a}\bar{m}_c$.

With these parameters defined, the equations describing the mass and composition of a magma chamber at time t are:

$$\frac{dM}{dt} = -\frac{dM_c}{dt} + \frac{dM_a}{dt} = -\bar{m}_c + \bar{m}_a = -\bar{m}_c(1 - \bar{a}) \quad (1)$$

$$\frac{dC_m}{dt} = \left(\frac{\bar{m}_c}{M}\right)[\bar{a}(C_a - C_m) - (D - 1)C_m] \quad (2)$$

$$\frac{d\varepsilon_m}{dt} = \left(\frac{\bar{m}_c}{M}\right)\left[\bar{a}\frac{C_a}{C_m}(\varepsilon_a - \varepsilon_m)\right] \quad (3)$$

Stepwise solutions for (1-3) can be written as:

$$M(t_n) = M(t_{n-1}) + \left(\frac{dM}{dt}\right)_{t_{n-1}} \Delta t \quad (4)$$

$$C_m(t_n) = C_m(t_{n-1}) + \left(\frac{dC_m}{dt}\right)_{t_{n-1}} \Delta t \quad (5)$$

$$\varepsilon_m(t_n) = \varepsilon_m(t_{n-1}) + \left(\frac{d\varepsilon_m}{dt}\right)_{t_{n-1}} \Delta t \quad (6)$$

In this stepwise formulation, total mass assimilated is:

$$M_a(t_n) = M_a(t_{n-1})(1 - M_c) + \left(\frac{dM_a}{dt}\right)_{t_{n-1}} \Delta t \quad (7)$$

The fraction of crustal assimilant in the magma chamber can be calculated by combining (4) and (7):

$$f_c(t_n) = \frac{M_a}{M}(t_n) \quad (8)$$

**5.4.2 Endmember compositions**

Isotopic compositions of both endmembers are shown in Table 3. For the parental magma, we estimate that $^{87}Sr/^{86}Sr = 0.7041$, $\varepsilon_{Nd} = 5.5$, and $^{208}Pb/^{206}Pb = 2.053$ (Figure 5). These values fall within the ranges observed in the Western Cordillera and back-arc where isotopically primitive compositions reflect limited assimilation of isotopically primitive Western Cordillera basement consisting of island arcs and oceanic plateaus (Ancellin et al., and references therein). The $\varepsilon_{Hf}$ value of 9.7 for the basaltic endmember was calculated using its $\varepsilon_{Nd}$ projected onto the $\varepsilon_{Hf}$-$\varepsilon_{Nd}$ terrestrial array (Figure 5; Vervoort et al., 2001).

Relative to the Reventador lavas, the assimilant must have high $^{87}Sr/^{86}Sr$ and $^{208}Pb/^{206}Pb$ as well as low $\varepsilon_{Nd}$ and $\varepsilon_{Hf}$. Since the basement samples analyzed in this study have $^{87}Sr/^{86}Sr$, $\varepsilon_{Nd}$, and $\varepsilon_{Hf}$ similar to or more primitive than the Reventador lavas, they do not represent the crustal assimilant. Instead, we estimate that crustal $^{87}Sr/^{86}Sr = 0.7200$ and

496 $\varepsilon_{Nd}$ = -10. These values were used to model evolution at Chalupas (Hammersley et al.
497 2022) and are comparable to the most evolved basement samples analyzed as part of that
498 study as well as model crust compositions from previous studies (Figure 5; Bryant et al.,
499 2006; Hidalgo et al., 2012). As with the parental basalts, we estimate $\varepsilon_{Hf}$ of the assimilant
500 by projecting its $\varepsilon_{Nd}$ onto the $\varepsilon_{Hf}$-$\varepsilon_{Nd}$ terrestrial array (Vervoort et al., 2001). Finally,
501 because few other studies have measured $^{208}Pb/^{206}Pb$ of potential assimilant lithologies
502 beneath NVZ, we define $^{208}Pb/^{206}Pb$ of the assimilant using sample SU-11, which has the
503 highest $^{208}Pb/^{206}Pb$ measured in the NVZ (Figure 5, Tables 1 and 3).
504 Unlike isotope ratios, the elemental concentrations of both endmembers, which we
505 refer to as $C_o$ and $C_a$ for the parental basalt and crustal assimilant, respectively, cannot be
506 easily estimated from previous studies. The concentrations of the basaltic endmember, $C_o$,
507 are particularly hard to define. Basalts are exceedingly rare in the NVZ, and have only been
508 collected at Sangay, the southernmost volcano, and in the back-arc. However, isotopic
509 analyses indicate that Sangay basalts have undergone crustal assimilation (Ancellin et al.,
510 2017), and major and trace element data suggest that the melt regimes in the NVZ main-
511 and back-arcs are different (Ancellin et al., 2017; Garrison et al., 2018). Consequently,
512 neither back-arc basalts nor Sangay basalts are analogous to the Reventador parental
513 basalts. Alternatively, $C_o$ values could be defined using basalts from other arcs or global
514 averages. However, arc basalts are incredibly diverse. Their compositions depend on
515 magma sources (i.e., compositions of the mantle wedge and subducting crust and sediment)
516 as well as the pressure and temperature of metasomatism and melting. Since these factors
517 are poorly constrained in the NVZ, it is difficult to determine whether basalts from other
518 arcs and global averages accurately reflect regional basalt compositions. The

519 concentrations of the assimilant, $C_a$, are similarly hard to define. This is due to the lack of
520 exposure, and also because the metamorphic basement in the NVZ is lithologically and
521 geochemically diverse (Hammersley et al., 2022).

522 Fortunately, if the isotopic compositions of the parental basalt and assimilant
523 endmembers are defined, then model isotope ratios are more sensitive to changes in the
524 concentration ratios of the endmembers, $C_o/C_a$, than individual concentrations themselves.
525 This is shown below:

526 $\varepsilon_m$ can also be expressed as a function of f, the current magma mass / initial magma mass

527 $$\varepsilon_m(f) = \frac{\left(\frac{\bar{a}}{\bar{a}-1}\right)\left(\frac{C_a}{z}\right)(1-f^{-z})\varepsilon_a + C_o f^{-z}\varepsilon_o}{\left(\frac{\bar{a}}{\bar{a}-1}\right)\left(\frac{C_a}{z}\right)(1-f^{-z}) + C_o f^{-z}} \quad (9; \text{DePaolo et al., 1981})$$

528 Where $z = \frac{\bar{a}+D-1}{\bar{a}-1}$. Differentiating Eq. 9 with respect to $C_o$ and $C_a$ yields the following:

529 $$\frac{\partial \varepsilon_m}{\partial C_o} = \frac{(\varepsilon_o - \varepsilon_a)\left(\frac{C_a}{z}\right)(f^{-z})\left(\frac{\bar{a}}{\bar{a}-1}\right)(1-f^{-z})}{\left(\left(\frac{\bar{a}}{\bar{a}-1}\right)\left(\frac{C_a}{z}\right)(1-f^{-z}) + C_o F^{-z}\right)^2} \quad (10)$$

530 $$\frac{\partial \varepsilon_m}{\partial C_a} = \frac{(\varepsilon_a - \varepsilon_o)\left(\frac{C_o}{z}\right)(f^{-z})\left(\frac{\bar{a}}{\bar{a}-1}\right)(1-f^{-z})}{\left(\left(\frac{\bar{a}}{\bar{a}-1}\right)\left(\frac{C_a}{z}\right)(1-f^{-z}) + C_o f^{-z}\right)^2} \quad (11)$$

531 These equations are almost identical, except that they have opposite signs, and Eq. (10) has
532 a $\frac{C_a}{z}$ term in the numerator while Eq. (11) has a $\frac{C_o}{z}$ term. Equations (10) and (11) can be
533 combined to give:

534 $$\frac{\partial \varepsilon_m}{\partial} = -\frac{\partial \varepsilon_m}{\partial C_o}\left(\frac{C_o}{C_a}\right) (12)$$

535 This demonstrates that 1) increasing $C_a$ and $C_o$ has opposite effects on $\varepsilon_m$; and 2)
536 for a given D, ā, and f (or $\varepsilon_m(t_n)$), $\varepsilon_m$ is constant if $\frac{C_o}{C_a}$ is constant. Therefore, instead of

varying both $C_a$ and $C_o$, we can fix the concentrations of one endmember, and examine how predicted isotope ratios change as a function of the other.

### 5.4.3 Depth of assimilation

While model results do not depend explicitly on the depth of assimilation, it is important to consider where assimilation occurs, as this affects ā as well as the crystallizing phases and resulting partition coefficients. Because Reventador lavas do not preserve petrographic evidence of assimilation such as crustal xenoliths, the depth of assimilation is unclear. While petrographic studies suggest that magmas are stored and homogenized in the upper crust at 7-12 km depth, there is no petrographic evidence indicating that assimilation also occurs at shallow depths (Ridolfi et al., 2008; Samaniego et al., 2008). In fact, significant amounts of assimilation are unlikely to occur in the upper crust because the crust is cooler, and more energy is required to heat the crust to its melting point, which limits the total amount of assimilation.

Instead, previous studies of continental arc magmatism suggest that assimilation is more likely to occur near the base of the crust. This region near the base of the crust has been referred to as the "MASH zone" (melting, assimilation, storage, and homogenization; Hildreth and Moorbath, 1988) or the "deep crustal hot zone" (Annen et al., 2006). At these depths the temperature difference between the parental magma and assimilant is minimized, and therefore the amount of energy required to heat the crust to its melting point is also minimized, which in turn maximizes ā and the amount of assimilation that occurs (DePaolo et al., 2019; Hammersley and DePaolo, 2006; Perry et al., 1992). Although the crust in the Eastern Cordillera is 50-55 km thick, gravity data indicates that

560 the lowermost ~10 km is composed of dense mafic material. Therefore, in this region
561 assimilation likely occurs at ~40 – 45 km depth (Asumpção et al., 2013; Condori et al.,
562 2017; Koch et al., 2021; Feineger and Seguin, 1993; Chulick et al., 2013; Hammersley et
563 al, 2022). However, without petrographic evidence or detailed studies of single crystals
564 (e.g. Ginibre and Davidson, 2014) we cannot confirm the depth of assimilation, and
565 therefore this process could conceivably occur at any depth throughout the crust.
566
567 **5.4.4 Model isotope ratios**
568 Model isotope ratios are shown in Figure 6. With $\bar{a} = 0.15$, 10 – 20% assimilation is
569 required to generate the compositional range observed in Reventador lavas. This value is
570 similar to estimates for the extent of crustal assimilation occurring at other Eastern
571 Cordillera volcanoes such as Chalupas (13.5 – 25%) and Cayambe (3 – 30%), but more
572 than Antisana (2.2 – 4.5 %) (Bourdon et al., 2002; Samaniego et al., 2005; Hammersley et
573 al., 2022).
574 Endmember compositions used in the model are shown in Table 3. Using the
575 average continental crust composition from Rudnick and Gao (2014) to approximate $C_a$, a
576 range of $C_o$ are needed to reproduce the full spectrum of isotopic diversity, which suggests
577 that the endmembers are somewhat heterogeneous (Minimum and maximum values given
578 in Table 3 form the gray shaded field in Figure 6). The model mineral assemblages and
579 partition coefficients used are shown in Table 4. Model A was produced via removal of a
580 gabbroic mineral assemblage consisting of 47.5 % olivine, 18.8% clinopyroxene, 9.4%
581 orthopyroxene, 18.8% plagioclase, 4.5% amphibole, and 1% garnet. Since Nd, Hf, and Pb
582 are incompatible in all fractionating phases, varying the mineral proportions has a small

583 effect on the bulk partitioning coefficients, and therefore does not affect $\varepsilon_{Nd}$, $\varepsilon_{Hf}$, and
584 $^{208}Pb/^{206}Pb$. However, since Sr is compatible in plagioclase, changing the amount of
585 plagioclase can account for additional variability of $^{87}Sr/^{86}Sr$. Increasing the amount of
586 plagioclase removed increases $D_{Sr}$ and vice versa. If ā, $^{87}Sr/^{86}Sr_a$, $^{87}Sr/^{86}Sr_o$, and $Sr_a/Sr_o$ are
587 held constant, increasing $D_{Sr}$ decreases $Sr_m(t)$ (equations 2 and 5), which in turn increases
588 $Sr_a/Sr_m$ and $\frac{d\varepsilon_{Sr}}{dt}$ (equation 3). This is illustrated in Figure 6. Models A, B, and C all have
589 $Sr_o$ = 1300 ppm and $Sr_a$ = 320 ppm. However, the model A assemblage contains 18.8 %
590 plagioclase, while model B contains 28.8 % plagioclase, and model C contains 8.8 %
591 plagioclase. Consequently, when compared with model A, model B predicts that $^{87}Sr/^{87}Sr$
592 changes more rapidly relative to other isotope ratios, while model C predicts less rapid
593 changes in $^{87}Sr/^{86}Sr$ (Figure 6).
594
595 **5.4.5 Model trace element ratios**
596 The origin of elevated LREE/HREE in NVZ lavas is widely debated. Some studies
597 attribute this trait to melting of subducted crust (e.g., Hidalgo et al., 2012), while others
598 suggest it is generated by assimilation (e.g., Garrison et al., 2006) or fractional
599 crystallization of garnet in the mantle and lower crust (e.g., Bloch et al., 2017; Bryant et al.,
600 2006, and references therein). Regardless, Reventador lavas show systematic covariance
601 between La/Yb, and Sr, Nd, Hf, and Pb isotope ratios indicating that interaction between
602 ascending magmas and the continental crust also increases LREE/HREE.
603 Since changes in $C_a$ are scaled by ā = 0.15 (equation 2), model trace element
604 concentrations are not highly sensitive to changes in the assimilant composition. This lack
605 of sensitivity is especially true for compatible elements, such as Yb when garnet and

amphibole are crystallizing. In this case, it is likely that $\bar{a}(C_a-C_m) << |(D-1)C_m|$ (equation 2), and thus the effects of assimilation will be negligible compared to the effects of fractional crystallization. Incompatible elements with mineral-melt partition coefficients approaching zero are slightly more sensitive to assimilation. However, unless $C_a-C_m$ is sufficiently large it is still likely that $\bar{a}(C_a-C_m) < C_m$, and thus changing $C_a$ has limited impact on model results. Therefore, we assume that $La/Yb_a = 10.5$ (Rudnick and Gao, 2014), and examine how changing the mineral assemblage and the parental basalt composition affect model results. With the model A mineral assemblage (Table 4), $La/Yb_o = 18 – 20$ is needed to reproduce the La/Yb of 21st century samples (Figure 8), which is comparable to the range found within primitive continental arc basalts from Mexico, The Cascades, and Central America (Schmidt and Jagoutz, 2015). However, increasing the amount of garnet in the mineral assemblage causes La/Yb to increase more quickly. Thus, lower $La/Yb_o$ can be compensated for with increased garnet crystallization and vice versa. This is shown in model D, which has $La/Yb_o = 15$ and 2% garnet. Compared to 21st century lavas, trends between La/Yb and radiogenic isotope ratios among 20th century lavas are weaker. However, Low La/Yb among 20th century lavas can be reproduced by further lowering $La/Yb_o$. Model E reproduces the 20th century compositions with the model A mineral assemblage and $La/Yb_o = 9–11$ (Figure 8).

Weak correlations between La/Sm and isotope ratios indicate that assimilation also increases LREE/MREE ratios (Figure 8). With $La/Sm_a = 5.13$ and $La/Sm_o = 4.5 – 5$, model A reproduces the full range of La/Sm found in Reventador lavas. However, since lavas with $^{238}U$-excesses have higher La/Sm than lavas with $^{230}Th$-excesses, and ($^{230}Th/^{238}U$)

does not vary systematically with isotope ratios or wt. % $SiO_2$, an additional mechanism is necessary to explain variable La/Sm.

### 5.4.6 $^{238}U$- $^{230}Th$ systematics

In many regards, ($^{230}Th/^{232}Th$) behaves similarly to the radiogenic isotope ratios described in Section 5.4.4. Although ingrowth and decay change ($^{230}Th/^{232}Th$), this ratio is not affected by high-temperature igneous processes. Consequently, ($^{230}Th/^{232}Th$) is sensitive to the ($^{230}Th/^{232}Th$) of the endmembers, $Th_a$, $Th_o$, and the time elapsed since establishment of disequilibrium. Since all phases included in the model have $D_{Th} << 1$, changing the fractionating assemblage does not significantly affect model results. We calculate $(^{230}Th/^{232}Th)_a = 0.706$ using average crustal Th and U concentrations and assuming secular equilibrium between ($^{238}U/^{232}Th$) and ($^{230}Th/^{232}Th$), and also assume that $Th_a = 1.2$ ppm (Rudnick and Gao, 2014). This value falls within the range of ($^{230}Th/^{232}Th$) calculated for the basement samples analyzed in this study, assuming secular equilibrium (Table 3). In contrast to the crustal endmember, ($^{230}Th/^{232}Th$) of the parental basalt is more difficult to define as it depends on the following processes which are poorly understood in the NVZ: 1) ($^{238}U/^{232}Th$) of the mantle and slab components; 2) U/Th elemental fractionation during metasomatism and melting; 3) ingrowth of $^{230}Th$ during melting; and 4) time elapsed between melting and assimilation (Reubi et al., 2014 and references therein). However, since assimilation lowers ($^{230}Th/^{232}Th$), we expect that $(^{230}Th/^{232}Th)_o >$ 1.173, the highest ($^{230}Th/^{232}Th$) measured among Cotopaxi Andesites (Garrison et al., 2006) Consequently, we estimate that $(^{230}Th/^{232}Th)_o = 1.2$. With these endmember compositions as well as the ā values and amount of crust assimilated defined above, $Th_o = 0.25 – 0.5$ is

required to reproduce the full range of ($^{230}Th/^{232}Th$) measured in Reventador lavas as well as the trends between ($^{230}Th/^{232}Th$) and radiogenic isotopes (Figure 10).

It is also important to consider the time elapsed since assimilation. Decay and ingrowth of $^{230}Th$ towards secular equilibrium could account for additional variability in ($^{230}Th/^{232}Th$) beyond that produced by varying $(^{230}Th/^{232}Th)_o$ and/or $Th_a/Th_o$. However, systematic variability between ($^{230}Th/^{232}Th$) and long-lived radiogenic isotope ratios (Figure 10) indicates that ($^{230}Th/^{232}Th$) is primarily a function of the parental magma's and assimilant's ($^{238}U/^{232}Th$), and that the effects of ingrowth and decay are secondary. Therefore, we suggest that assimilation occurred within a few tens of thousands of years. This finding is consistent with previous studies suggesting that assimilation occurs on timescales that are fast relative to the half-life of $^{230}Th$ (Hora et al., 2009; Handley et al., 2008; Jicha et al., 2007; Price et al., 2007)

We also examine the effects of assimilation on ($^{230}Th/^{238}U$) and ($^{238}U/^{232}Th$). Changing the mineral assemblage does not significantly affect the modeled ($^{238}U/^{232}Th$) or ($^{230}Th/^{238}U$). Since the phases included in our modelling all have $D_U$ and $D_{Th} << 1$, very little U and Th are removed from the magma. Consequently, the modelled ($^{238}U/^{232}Th$) and ($^{230}Th/^{238}U$) are more sensitive to changes in endmember compositions than phase proportions. As such, we suggest that variable ($^{238}U/^{232}Th$) and ($^{230}Th/^{238}U$) > 1 result from heterogeneous endmember compositions. Previous studies have shown that assimilation of partial melts with ($^{230}Th/^{238}U$) > 1 can produce intermediate-felsic lavas with $^{230}Th$-excess (Ankenny et al., 2013; Berlo et al., 2004; Cooper et al., 2002; Garrison et al., 2006). However, if ($^{230}Th/^{238}U$) of the parental basalt and assimilant are fixed, then ($^{238}U/^{232}Th$) would vary systematically with other isotope ratios or wt. % $SiO_2$, which is not observed.

674 Therefore, an additional mechanism is required to produce the observed diversity. We posit
675 that the most likely explanation is that the crustal assimilant and parental magma have
676 heterogeneous ($^{238}U/^{232}Th$) and ($^{230}Th/^{238}U$), reflecting differences in the extent of melting
677 and metasomatism as well as the metasomatic agent (i.e. fluid vs. melt, Kessel et al., 2005)
678 as well as differences in the degree of crustal melting. For instance, with $(^{230}Th/^{232}Th)_o$ =
679 1.2, $(^{230}Th/^{232}Th)_a$ = 0.706, $Th_a$ = 1.2, and $Th_o$ = 0.32, Reventador lavas with $(^{230}Th/^{238}U)$ >
680 1 can be generated with $(^{230}Th/^{238}U)_a$ = 1.1–1.3 and $(^{230}Th/^{238}U)_o$ = 0.95–1.05 (Figure 12).
681 With the $(^{230}Th/^{232}Th)_o$, $(^{230}Th/^{232}Th)_a$, $Th_a/Th_o$, and $(^{230}Th/^{238}U)_a$ values outlined
682 above, $^{238}U$-excess in a subset of lavas can be accounted for by extending $(^{230}Th/^{238}U)_o$ to
683 0.8–0.9 (Figure 12). Since U is more mobile than Th in aqueous fluids, lower $(^{230}Th/^{238}U)_o$
684 may reflect increased involvement of aqueous fluids during metasomatism. This
685 explanation is supported by higher Pb/Ce in lavas with $^{238}U$-excess, as Pb is more mobile in
686 fluids than Ce (Figure 11). Although La/Sm is also influenced by assimilation (section
687 5.4.5), this mechanism could also produce higher La/Sm observed in samples with $^{238}U$-
688 excess (Figure 11; Kessel et al., 2005). However, this explanation is difficult to verify with
689 our current understanding of basalt petrogenesis in the NVZ.
690 Although model ($^{238}U/^{230}Th$) and ($^{230}Th/^{238}U$) are more sensitive to endmember
691 compositions than mineral assemblage (see above), we also examine the effects of
692 crystallization of accessory minerals with $D_U < D_{Th}$. Garrison et al. (2006) suggested that
693 crystallization of a phase assemblage containing 5% apatite results in $^{238}U$-excesses among
694 Cotopaxi rhyolites. Since apatite also has $D_{Pb} < D_{Ce}$ and $D_{La} < D_{Sm}$, removal of this phase
695 could potentially explain the elevated Pb/Ce and La/Sm of lavas with $^{238}U$-excess
696 (Prowatke and Klemme, 2006). However, Reventador lavas contain only trace apatite,

697 which limits the amount of apatite in the crystallizing assemblage (Ridolfi et al., 2008).
698 Although adding 1% apatite decreases $D_U/D_{Th}$ from 0.96 to 0.51, $D_U$ and $D_{Th}$ remain << 1.
699 Consequently, apatite crystallization is unlikely to produce the observed $^{238}$U-excess in a
700 few Reventador lavas. As such, we argue that variable $^{230}$Th-$^{238}$U disequilibria result
701 primarily from source heterogeneity.
702
703 **5.4.7 Comparison of the Finite Difference- and Energy Constrained Assimilation**
704 **Fractional Crystallization Models**
705 Since the development of the AFC model (DePaolo, 1981), numerous other
706 formulations have been proposed, most notably, the Energy Constrained AFC model (EC-
707 AFC; Spera and Bohrson, 2001; Bohrson and Spera, 2001). The primary difference
708 between the FD-AFC and the EC-AFC models is that the EC-AFC model accounts for the
709 thermodynamics of the system. So, in principle, the EC-AFC model is more realistic, as
710 long as the lithology and thermal structure of the assimilation crust are known explicitly.
711 The main difference of the EC-AFC model is that the ratio of mass assimilated
712 /mass crystallized ($M_a/M_c$ or ā) changes continuously, whereas in the FD-AFC model this
713 parameter is constant, unless the user changes it stepwise. In the EC-AFC model, the user
714 must define the equilibration temperature, $T_{eq}$, which controls the extent of interaction
715 between the parental magma and assimilant, and therefore the total amount of crust
716 assimilated (Spera and Bohrson, 2001). To set $T_{eq}$, the thermal structure of the crust as well
717 as the depth of assimilation must be well constrained. The EC-AFC model also accounts
718 for partial melting of the crust by allowing the user to specify $K_D$ values for crustal melting.
719 In contrast, FD-AFC does not account for melting, and essentially $K_D = 1$, which

720 approximates bulk assimilation of the crust. While the inclusion of partial melting is more
721 realistic, setting $K_D$ appropriately requires that the user have a clear idea of the crustal
722 lithology. Thus, when using EC-AFC, the modeler must know both the lithological
723 composition of the crust being assimilated and the equilibration temperature, $T_{eq}$. As such,
724 the EC-AFC model is only as accurate as one's knowledge of the crust-magma system.
725 However, for Reventador, we lack explicit knowledge of the crustal lithology and
726 thermal structure. While studies suggest that assimilation occurs at ~40 – 45 km in the
727 NVZ (Asumpção et al., 2013; Condori et al., 2017; Koch et al., 2021; Feineger and Seguin,
728 1993; Chulick et al., 2013; Hammersley et al, 2022), Reventador lavas do not preserve
729 petrographic evidence of assimilation, and therefore we cannot definitively constrain either
730 the depth of assimilation or $T_{eq}$. As a result, the EC-AFC results are not necessarily more
731 accurate than the FD-AFC results. The advantage of FD-AFC is its simplicity; results
732 depend only on the ratio of mass assimilated/mass crystallized at each step, the
733 composition of the endmembers, and the crystallizing phases. Furthermore, when fitting the
734 model to the data, the assumption that D = 1 can be compensated for by changing the $C_a$ (or
735 $C_o$, since results depend on the ratio of $C_a$ to $C_o$) to reflect increased concentrations of
736 incompatible elements in the crustal melt. Additionally, the user can make incremental
737 steps that change the Ma/Mc stepwise.
738 Figure 13 compares the FD-AFC results shown in Figure 6 (model A) along with
739 results produced using EC-AFC of Spera and Bohrson (2001). In both models, we use the
740 same endmember compositions and partition coefficients for crystallization. We set the
741 thermal parameters for the EC-AFC model using the standard lower crustal parameters
742 listed in Bohrson and Spera (2001), and for the sake of comparison we also set D = 1 for all

743 elements during crustal melting. In the EC-AFC model we set the equilibration temperature
744 to 1228°C. This value was chosen because with the parameters listed above, equilibration
745 at 1228°C would yield ~20% assimilation, the amount of assimilation required by the FD-
746 AFC model to produce the trends observed in Reventador lavas. The main difference
747 between the two models is the amount of crust assimilated. While the FD-AFC model
748 reproduces the observed trends with 10-20% assimilation, the EC-AFC model requires less
749 assimilation, 8-12%. The slight divergence between the two models is due to the
750 differences in mass assimilated/mass crystallized at each step, which affects model
751 concentrations of each element differently, depending on $C_o/C_a$ ratios. Since model isotope
752 ratios depend on model concentrations, this effect carries over to model isotope ratios
753 (Figure 13). The divergence between the two models is largest when comparing trends
754 between isotope ratios whose elements have large differences in $C_o/C_a$. For instance, the
755 models in Figure 13 have $Sr_o/Sr_a = 4.1$, $Nd_o/Nd_a = 0.41$, $Hf_o/Hf_a = 0.41$, and $Pb_o/Pb_a = 0.16$
756 (Table 3). While the differences between the models are largest when comparing trends in
757 $^{87}Sr/^{86}Sr$ vs $\varepsilon_{Nd}$ or $^{206}Pb/^{208}Pb$, the difference is less pronounced in trends between $\varepsilon_{Nd}$ vs
758 $^{208}Pb/^{206}Pb$, and nearly nonexistent in $\varepsilon_{Nd}$ vs $\varepsilon_{Hf}$. Regardless, the significance of this
759 difference is small, considering that the lithology and thermal structure of the crust beneath
760 Reventador are poorly constrained. As understanding of the magmatic system at
761 Reventador evolves, we may be able to make the assumptions necessary to apply more
762 realistic and more complex models. However, with our current, limited, understanding of
763 the magmatic system, the FD-AFC model also demonstrates that crustal assimilation can
764 reproduce the observed isotopic trends.
765

## *6. Conclusions*

In this study, we show that assimilation significantly impacts magma composition at Reventador. Our finite difference-AFC modeling indicates that observed linear trends between radiogenic Sr, Nd, Hf and Pb isotopes, ($^{230}Th/^{232}Th$), LREE/HREE ratios (e.g., La/Yb) and LREE/MREE ratios (e.g., La/Sm) can be accounted for by 10-20% assimilation accompanied by fractional crystallization of a gabbroic assemblage. However, the full spectrum of isotopic and geochemical diversity of Reventador's lavas, including both $^{238}U$- and $^{230}Th$-excesses, also requires source heterogeneity. This additional heterogeneity most likely reflects variable degrees of metasomatism and melting during basalt petrogenesis as well as variable extents of crustal melting. In our FD-AFC models presented here, this variable source composition is demonstrated by the need to vary elemental concentrations in the parental magma ($C_o$).

Lastly, we compare coupled assimilation fractional crystallization models, explicitly Finite Difference-AFC and Energy Constrained-AFC models. Our comparison shows that while the EC-AFC model accounts for the thermodynamics of the system and is thus more realistic, the EC-AFC model is only as accurate as one's knowledge of the lithological composition of the crust being assimilated, the crust's thermal structure and the depth of assimilation; these parameters are often not well known for many continental crustal volcanic systems. In contrast, the FD-AFC model, albeit thermally simplistic, provides results that depend only on the ratio of mass assimilated/mass crystallized at each step, the composition of the endmembers, and the crystallizing phases.

While this study is specific to Reventador, its implications are global, providing an unprecedented understanding of the impact of assimilation of thickened and evolved

continental crust. Specifically, we demonstrate that crustal assimilation can overprint $^{238}$U-series signatures imparted during metasomatism and mantle melting. Consequently, $^{238}$U-series data cannot be interpreted in a vacuum, and must be considered in tandem with other data, especially long-lived radiogenic isotope ratios, which provide unambiguous information on long-term source variations.

***Acknowledgments***

This work was funded by NSF grants EAR 1019545 (KWWS) and EAR 1019546 (JMG). LBK acknowledges support from the Richard B. and Lynne V. Cheney Study-Abroad Scholarship Fund and the Center for Global Studies Excellence Fund at the University of Wyoming. KWWS acknowledges support from the US and Ecuadorian Fulbright Commissions as well as the National Geographic Society. LBK and KWWS both acknowledge Mark Thurber for his support in the field. JBT acknowledges financial support from the French Agence Nationale de la Recherche (grant ANR-10-BLAN-0603 M&Ms—Mantle Melting—Measurements, Models, Mechanisms). We also thank editor Rosemary Hickey-Vargas, Wendy Bohrson, Heye Freymuth, and two anonymous reviewers for their thoughtful feedback which improved this manuscript.

## Appendix A: Supplementary Material

There are four supplemental files associated with this manuscript. The first supplemental file is a table containing major and trace element data for Reventador lavas. The second file is a table containing regional data used in Figures two, three, four, and five. The third file is a document containing the citations for the sources of regional data. The fourth file contains supplemental material regarding the methods used in this study, as well as quality assurance data.

## References


Almeida, M., Gaunt, E., Ramon, P., 2019. Ecuador's El Reventador Volcano Continually Remakes Itself. *Eos Trans. AGU* **100**, 2019EO117105.

Ancellin, M.-A., Samaniego, P., Vlastelic, I., Nauret, F., Gannoun, A., Hidalgo, S., 2017. Across-arc versus along-arc Sr-Nd-Pb isotope variations in the Ecuadorian volcanic arc. *Geochem. Geophys. Geosyst.* **18**, 2016GC006679.

Ankney, M.E., Johnson, C.M., Bacon, C.R., Beard, B.L., Jicha, B.R., 2013. Distinguishing lower and upper crustal processes in magmas erupted during the buildup to the 7.7 ka climactic eruption of Mount Mazama, Crater Lake, Oregon, using 238U–230Th disequilibria. *Contrib. Mineral. Petrol.* **166**, 563–585.

Annen, C., Blundy, J.D., Sparks, R.S.J., 2006. The Genesis of Intermediate and Silicic Magmas in Deep Crustal Hot Zones. *J. Petrol.* **47**, 505–539.

Assumpção, M., Feng, M., Tassara, A., Julià, J., 2013. Models of crustal thickness for South America from seismic refraction, receiver functions and surface wave tomography. *Tectonophysics* **609**, 82–96.

Baize, S., Audin, L., Alvarado, A., Jomard, H., Bablon, M., Champenois, J., Espin, P., Samaniego, P., Quidelleur, X., Le Pennec, J.-L., 2020. Active Tectonics and Earthquake Geology Along the Pallatanga Fault, Central Andes of Ecuador. *Front. Earth Sci.* **8**, 2020.00193.

Ball, L., Sims, K.W.W., Schwieters, J., 2008. Measurement of $^{234}U/^{238}U$ and $^{230}Th/^{232}Th$ in volcanic rocks using the Neptune MC-ICP-MS. *J. Anal. At. Spectrom.* **23**, 173–180.

Berlo, K., Turner, S., Blundy, J., Hawkesworth, C., 2004. The extent of U-series disequilibria produced during partial melting of the lower crust with implications for the formation of the Mount St. Helens dacites. *Contrib. Mineral. Petrol.* **148**, 122–130.

Bindeman, I.N., Davis, A.M., 2000. Trace element partitioning between plagioclase and melt: investigation of dopant influence on partition behavior. *Geochim. Cosmochim. Acta* **64**, 2863–2878.

Bloch, E., Ibañez-Mejia, M., Murray, K., Vervoort, J., Müntener, O., 2017. Recent crustal foundering in the Northern Volcanic Zone of the Andean arc: Petrological insights from the roots of a modern subduction zone. *Earth Planet. Sci. Lett.* **476**, 47–58.

Bohrson, W.A., Spera, F.J., 2001. Energy-Constrained Open-System Magmatic Processes II: Application of Energy-Constrained Assimilation–Fractional Crystallization (EC-AFC) Model to Magmatic Systems. *J. Petrol.* **42**, 1019–1041.

Bourdon, B., Sims, K.W.W., 2003. U-series Constraints on Intraplate Basaltic Magmatism. *Rev. Mineral. Geochem.* **52**, 215–254.

Bourdon, B., Turner, S., Henderson, G.M., Lundstrom, C.C., 2003. Introduction to U-series *Geochemistry. Rev. Mineral. Geochem.* **52**, 1–21.

Bourdon, B., Turner, S.P., Ribe, N.M., 2005. Partial melting and upwelling rates beneath the Azores from a U-series isotope perspective. *Earth Planet. Sci. Lett.* **239**, 42–56.

Bourdon, B., Wörner, G., Zindler, A., 2000. U-series evidence for crustal involvement and magma residence times in the petrogenesis of Parinacota volcano, Chile. *Contrib. Mineral. Petrol.* **139**, 458–469.

Bourdon, B., Zindler, A., Elliott, T., Langmuir, C.H., 1996. Constraints on mantle melting at mid-ocean ridges from global $^{238}U$-$^{230}Th$ disequilibrium data. *Nature* **384**, 231–235

Bourdon, E., Eissen, J., Monzier, M., Robin, C., Martin, H., Cotten, J., Hall, M.L., 2002. Adakite-like lavas from Antisana Volcano (Ecuador): evidence for slab melt metasomatism beneath Andean Northern Volcanic Zone. *J. Petrol.* **43**, 199–217.

Bourdon, E., Eissen, J.-P., Gutscher, M.-A., Monzier, M., Hall, M.L., Cotten, J., 2003. Magmatic response to early aseismic ridge subduction: the Ecuadorian margin case (South America). *Earth Planet. Sci. Lett.* **205**, 123–138.

Bryant, J.A., Yogodzinski, G.M., Hall, M.L., Lewicki, J.L., Bailey, D.G., 2006. Geochemical Constraints on the Origin of Volcanic Rocks from the Andean Northern Volcanic Zone, Ecuador. *J. Petrol.* **47**, 1147–1175.

Chiaradia, M., 2009. Adakite-like magmas from fractional crystallization and melting-assimilation of mafic lower crust (Eocene Macuchi arc, Western Cordillera, Ecuador). *Chem. Geol.* **265**, 468–487.

Chiaradia, M., Fontboté, L., Paladines, A., 2004. Metal Sources in Mineral Deposits and Crustal Rocks of Ecuador (1° N–4° S): A Lead Isotope Synthesis. *Econ. Geol.* **99**, 1085–1106.

Chiaradia, M., Müntener, O., Beate, B., 2020. Effects of aseismic ridge subduction on the geochemistry of frontal arc magmas. *Earth Planet. Sci. Lett.* **531**, 2019.115984.

Chiaradia, M., Müntener, O., Beate, B., 2011. Enriched Basaltic Andesites from Mid-crustal Fractional Crystallization, Recharge, and Assimilation (Pilavo Volcano, Western Cordillera of Ecuador). *J. Petrol.* **52**, 1107–1141.

Chiaradia, M., Müntener, O., Beate, B., Fontignie, D., 2009. Adakite-like volcanism of Ecuador: lower crust magmatic evolution and recycling. *Contrib. Mineral. Petrol.* **158**, 563–588.

Chulick, G.S., Detweiler, S., Mooney, W.D., 2013. Seismic structure of the crust and uppermost mantle of South America and surrounding oceanic basins. *J. S. Am. Earth Sci.* **42**, 260–276.

Condori, C., França, G.S., Tavera, H.J., Albuquerque, D.F., Bishop, B.T., Beck, S.L., 2017. Crustal structure of north Peru from analysis of teleseismic receiver functions. *J. S. Am. Earth Sci.* **76**, 11–24.

Cooper, K.M., Reid, M.R., Dunbar, N.W., McIntosh,W.C., 2002. Origin of mafic magmas beneath northwestern Tibet: Constraints from $^{230}$Th-$^{238}$U disequilibria. *Geochem. Geophys. Geosyst.* **3**, 1–23.

Davidson, J.P., Hora, J.M., Garrison, J.M., Dungan, M.A., 2005. Crustal forensics in arc magmas. *J. Volcanol. Geotherm. Res*.**140**, 157–170.

Defant, M.J., Drummond, M.S., 1990. Derivation of some modern arc magmas by melting of young subducted lithosphere. *Nature* **347**, 662–665.

DePaolo, D.J., 1985. Isotopic studies of processes in mafic magma chambers: I. The Kiglapait Intrusion, Labrador. *J. Petrol.* **26**, 925–951.

DePaolo, D.J., 1981. Trace element and isotopic effects of combined wallrock assimilation and fractional crystallization. *Earth Planet. Sci. Lett.* **53**, 189–202.

DePaolo, D.J., Harrison, T.M., Wielicki, M., Zhao, Z., Zhu, D.C., Zhang, H., Mo, X., 2019. Geochemical evidence for thin syn-collision crust and major crustal thickening

between 45 and 32 Ma at the southern margin of Tibet. *Gondwana Res.* **73**, 123–135.

Dostal, J., Dupuy, C., Carron, J.P., le Guen de Kerneizon, M., Maury, R.C., 1983. Partition coefficients of trace elements: Application to volcanic rocks of St. Vincent, West Indies. *Geochim. Cosmochim. Acta* **47**, 525–533.

DuFrane, S.A., Turner, S., Dosseto, A., Soest, M. van, 2009. Reappraisal of fluid and sediment contributions to Lesser Antilles magmas. *Chem. Geol.* **265**, 272–278.

Dunn, T., Sen, C., 1994. Mineral/matrix partition coefficients for orthopyroxene, plagioclase, and olivine in basaltic to andesitic systems: A combined analytical and experimental study. *Geochim. Cosmochim. Acta* **58**, 717–733.

Elkins, L.J., Sims, K.W.W., Prytulak, J., Blichert-Toft, J., Elliott, T., Blusztajn, J., Fretzdorff, S., Reagan, M., Haase, K., Humphris, S., 2014. Melt generation beneath Arctic Ridges: Implications from U decay series disequilibria in the Mohns, Knipovich, and Gakkel Ridges. *Geochim. Cosmochim. Acta* **127**, 140–170.

Elkins, L.J., Sims, K.W.W., Prytulak, J., Elliott, T., Mattielli, N., Blichert-Toft, J., Blusztajn, J., Dunbar, N., Devey, C., Mertz, D.F., Schilling, J.-G., Murrell, M., 2011. Understanding melt generation beneath the slow-spreading Kolbeinsey Ridge using $^{238}$U, $^{230}$Th, and $^{231}$Pa excesses. *Geochim. Cosmochim. Acta* **75**, 6300–6329.

Elliott, T., Plank, T., Zindler, A., White, W., Bourdon, B., 1997. Element transport from slab to volcanic front at the Mariana arc. *J. Geophys. Res. Solid Earth* **102**, 14991–15019.

Feininger, T., Seguin, M.K., 1983. Simple Bouguer gravity anomaly field and the inferred crustal structure of continental Ecuador. *Geology* **11**, 40-44.

Garrison, J., Davidson, J., Reid, M., Turner, S., 2006. Source versus differentiation controls on U-series disequilibria: Insights from Cotopaxi Volcano, Ecuador. *Earth Planet. Sci. Lett.* **244**, 548–565.

Garrison, J., Sims, K.W.W., Yogodzinski, G., Escobar, R., Scott, S., Mothes, P., Hall, M., Ramon, P., 2018. Shallow-level differentiation of phonolitic lavas from Sumaco Volcano, Ecuador. *Contrib. Mineral. Petrol.* **173**, 1–19.

Garrison, J.M., Davidson, J.P., 2003. Dubious case for slab melting in the Northern volcanic zone of the Andes. *Geology* **31**, 565–568.

George, R., Turner, S., Hawkesworth, C., Morris, J., Nye, C., Ryan, J., Zheng, S.-H., 2003. Melting processes and fluid and sediment transport rates along the Alaska-Aleutian arc from an integrated U-Th-Ra-Be isotope study. *J. Geophys. Res. Solid Earth* **108**, 2002JB001916.

Gerlach, D.C., Frey, F.A., Moreno-roa, H., Lopez-escobar, L., 1988. Recent Volcanism in the Puyehue—Cordon Caulle Region, Southern Andes, Chile (40·5°S): Petrogenesis of Evolved Lavas. *J. Petrol.* **29**, 333–382.

Ginibre, C., Davidson, J.P., 2014. Sr Isotope Zoning in Plagioclase from Parinacota Volcano (Northern Chile): Quantifying Magma Mixing and Crustal Contamination. J. *Petrol*. **55**, 1203–1238.

Gutscher, M.-A., Maury, R., Eissen, J.-P., Bourdon, E., 2000. Can slab melting be caused by flat subduction? *Geology* **28**, 535–538.

Goldstein, S.J., Murrell, M.T., Janecky, D.R., 1989. Th and U isotopic systematics of basalts from the Juan de Fuca and Gorda Ridges by mass spectrometry. *Earth Planet. Sci. Lett.* **96**, 134–146.

Goldstein, S.J., Murrell, M.T., Janecky, D.R., Delaney, J.R., Clague, D.A., 1992. Geochronology and petrogenesis of MORB from the Juan de Fuca and Gorda ridges by $^{238}$U-$^{230}$Th disequilibrium. *Earth Planet. Sci. Lett.* **109**, 255–272.

Goldstein, S.J., Murrell, M.T., Williams, R.W., 1993. $^{231}$Pa and $^{230}$Th chronology of mid-ocean ridge basalts. *Earth Planet. Sci. Lett.* **115**, 151–159.

Hall, M., Ramón, P., Mothes, P., LePennec, J.L., García, A., Samaniego, P., Yepes, H., 2004. Volcanic eruptions with little warning: the case of Volcán Reventador's Surprise November 3, 2002 Eruption, Ecuador. *Revista geológica de Chile* **31**, 349–358.

Hall, M.L., Samaniego, P., Pennec, J.L. le, Johnson, J.B., 2008. Ecuadorian Andes volcanism: A review of Late Pliocene to present activity. *J. Volcanol. Geotherm. Res.* **176**, 1-6.

Hammersley, L., DePaolo, D.J., 2006. Isotopic and geophysical constraints on the structure and evolution of the Clear Lake volcanic system. *J. Volcanol. Geotherm. Res.* **153**, 331–356.

Hammersley, L., DePaolo, D.J., Beate, B., and Deino, L.A., 2022. Rhyolite Ignimbrite generation in the Northern Andes: The Chalupas Caldera, Ecuador. In *Isotopic Constraints on Earth System Processes* (eds. K.W.W. Sims, K. Maher, and D.P. Schrag). American Geophysical Union, Geophysical Monography Series. pp. 87-132. 10.1002/9781119595007

Handley, H.K., Reagan, M., Gertisser, R., Preece, K., Berlo, K., McGee, L.E., Barclay, J., Herd, R., 2018. Timescales of magma ascent and degassing and the role of crustal assimilation at Merapi volcano (2006–2010), Indonesia: Constraints from uranium-

series and radiogenic isotopic compositions. *Geochim. Cosmochim. Acta* **222**, 34–52.

Harpp, K.S., White, W.M., 2001. Tracing a mantle plume: Isotopic and trace element variations of Galápagos seamounts. *Geochem. Geophys. Geosyst.* **2**, 2000GC000137.

Harpp, K.S., Wanless, V.D., Otto, R.H., Hoernle, K., Werner, R., 2005. The Cocos and Carnegie Aseismic Ridges: a Trace Element Record of Long-term Plume–Spreading Center Interaction. *J. Petrol.* **46**, 109–133.

Hart, S.R., Blusztajn, J., 2006. Age and geochemistry of the mafic sills, ODP site 1276, Newfoundland margin. *Chem. Geol.* **235**, 222–237.

Hart, S.R., Coetzee, M., Workman, R.K., Blusztajn, J., Johnson, K.T.M., Sinton, J.M., Steinberger, B., Hawkins, J.W., 2004. Genesis of the Western Samoa seamount province: Age, geochemical fingerprint and tectonics. *Earth Planet. Sci. Lett.* **227**, 37–56.

Hauri, E.H., Wagner, T.P., Grove, T.L., 1994. Experimental and natural partitioning of Th, U, Pb and other trace elements between garnet, clinopyroxene and basaltic melts. *Chem. Geol.* **117**, 149–166.

Hidalgo, S., Gerbe, M.C., Martin, H., Samaniego, P., Bourdon, E., 2012. Role of crustal and slab components in the Northern Volcanic Zone of the Andes (Ecuador) constrained by Sr–Nd–O isotopes. *Lithos* **132–133**, 180–192.

Hildreth, W., Moorbath, S., 1988. Crustal contributions to arc magmatism in the Andes of Central Chile. *Contrib. Mineral. Petrol.* **98**, 455–489.

Hora, J.M., Singer, B.S., Wörner, G., Beard, B.L., Jicha, B.R., Johnson, C.M., 2009. Shallow and deep crustal control on differentiation of calc-alkaline and tholeiitic magma. *Earth Planet. Sci. Lett.* **285**, 75–86.

Huang, F., Gao, L., Lundstrom, C.C., 2008. The effect of assimilation, fractional crystallization, and ageing on U-series disequilibria in subduction zone lavas. *Geochim. Cosmochim. Acta* **72**, 4136–4145.

Jackson, M. G., and Dasgupta, R., 2008. Compositions of HIMU, EM1, and EM2 from global trends between radiogenic isotopes and major elements in ocean island basalts. *Earth Planet. Sci. Lett.* **276**, 175–186.

Jaillard, E., Lapierre, H., Ordoñez, M., Álava, J.T., Amórtegui, A., Vanmelle, J., 2009. Accreted oceanic terranes in Ecuador: southern edge of the Caribbean Plate? In *The Origin and Evolution of the Caribbean Plate* (eds. K.H. James, M.A. Lorenth and J.A. Pindell) Geol. Soc., London, Special Publications 328. pp. 469-485.

Jarvis, K.E., 1988. Inductively coupled plasma mass spectrometry: A new technique for the rapid or ultra-trace level determination of the rare-earth elements in geological materials. *Chem. Geol.* **68**, 31–39.

Jicha, B.R., Johnson, C.M., Hildreth, W., Beard, B.L., Hart, G.L., Shirey, S.B., Singer, B.S., 2009. Discriminating assimilants and decoupling deep- vs. shallow-level crystal records at Mount Adams using $^{238}U$–$^{230}Th$ disequilibria and Os isotopes. *Earth Planet. Sci. Lett.* **277**, 38–49.

Jicha, B.R., Singer, B.S., Beard, B.L., Johnson, C.M., Moreno-Roa, H., Naranjo, J.A., 2007. Rapid magma ascent and generation of $^{230}Th$ excesses in the lower crust at Puyehue–Cordón Caulle, Southern Volcanic Zone, Chile. *Earth Planet. Sci. Lett.* **255**, 229–242.

Johnson, D.M., Hooper, P.R., Conrey, R.M., 1999. XRF analysis of rocks and minerals for major and trace elements on a single low dilution Li-tetraborate fused bead. *Adv. X Ray Anal*. **41**, 843–867.

Jull, M., Kelemen, P.B., Sims, K.W.W, 2002. Consequences of diffuse and channelled porous melt migration on uranium series disequilibria. Geochim Cosmochim Acta 66, 4133–4148. https://doi.org/10.1016/S0016-7037(02)00984-5

Kelley, K.A., Cottrell, E., 2009. Water and the oxidation state of subduction zone magmas. *Science* **325**, 605–607.

Kelley, K.A., Plank, T., Farr, L., Ludden, J., Staudigel, H., 2005. Subduction cycling of U, Th, and Pb. *Earth Planet. Sci. Lett.* **234**, 369–383.

Kessel, R., Schmidt, M.W., Ulmer, P., Pettke, T., 2005. Trace element signature of subduction-zone fluids, melts and supercritical liquids at 120–180 km depth. *Nature* **437**, 724–727.

Klein, M., Stosch, H.G., Seck, H.A., Shimizu, N., 2000. Experimental partitioning of high field strength and rare earth elements between clinopyroxene and garnet in andesitic to tonalitic systems. *Geochim. Cosmochim. Acta* **64**, 99–115.

Koch, C.D., Delph, J., Beck, S.L., Lynner, C., Ruiz, M., Hernandez, S., Samaniego, P., Meltzer, A., Mothes, P., Hidalgo, S., 2021. Crustal thickness and magma storage beneath the Ecuadorian arc. *J. S. Am. Earth Sci.* **110**, 2021.103331.

Kokfelt, T.F., Lundstrom, C., Hoernle, K., Hauff, F., Werner, R., 2005. Plume-ridge interaction studied at the Galápagos spreading center: Evidence from $^{226}Ra$-$^{230}Th$-$^{238}U$ and $^{231}Pa$-$^{235}U$ isotopic disequilibria. *Earth Planet. Sci. Lett.* **234**, 165–187.

Kuritani, T., Yokoyama, T., Nakamura, E., 2008. Generation of Rear-arc Magmas Induced by Influx of Slab-derived Supercritical Liquids: Implications from Alkali Basalt Lavas from Rishiri Volcano, Kurile Arc. *J. Petrol.* **49**, 1319–1342.

Layne, G.D. and K.W.W. Sims (2000). *Analysis of $^{232}Th/^{230}Th$ in volcanic rocks by Secondary Ionization Mass Spectrometry. Int. J. Mass Spectrom.* **203**, 1-3, 187-198.

Lundstrom, C.C., Gill, J., Williams, Q., Perfit, M.R., 1995. Mantle Melting and Basalt Extraction by Equilibrium Porous Flow. *Science* **270**, 1958-1961.

Lundstrom, C.C., Sampson, D.E., Perfit, M.R., Gill, J., Williams, Q., 1999. Insights into mid- ocean ridge basalt petrogenesis: U- series disequilibria from the Siqueiros Transform, Lamont Seamounts, and East Pacific Rise. *J. Geophys. Res. Solid Earth* **104**, 13035–13048.

McDonough, W.F., Sun, S.-S., 1995. The composition of the Earth. *Chem. Geol.* **120**, 223–253.

McKenzie, D., 1985. The extraction of magma from the crust and mantle. *Earth Planet. Sci. Lett.* **74**, 81–91.

McKenzie, D., O'Nions, R.K., 1991. Partial Melt Distributions from Inversion of Rare Earth Element Concentrations. *J. Petrol.* **32**, 1021–1091.

Michaud, F., Witt, C., Royer, J.-Y., 2009. Influence of the subduction of the Carnegie volcanic ridge on Ecuadorian geology: Reality and fiction. In *Backbone of the Americas: Shallow Subduction, Plateau Uplift, and Ridge and Terrane Collision* (eds. S.M. Kay, V.A. Ramos, W.R. Dickinson). Geol. Soc. Am., Boulder. pp. 217-228.

Miyashiro, A., 1974. Volcanic rock series in island arcs and active continental margins. *Am. J. Sci.* **274**, 321–355.

Münker, C., Weyer, S., Scherer, E., Mezger, K., 2001. Separation of high field strength elements (Nb, Ta, Zr, Hf) and Lu from rock samples for MC- ICPMS measurements. *Geochem. Geophys. Geosyst.* **2**. 2001GC000183.

Müntener, O., Kelemen, P.B., Grove, T.L., 2001. The role of $H_2O$ during crystallization of primitive arc magmas under uppermost mantle conditions and genesis of igneous pyroxenites: an experimental study. *Contrib. Mineral. Petrol.* **141**, 643–658.

Nandedkar, R.H., Hürlimann, N., Ulmer, P., Müntener, O., 2016. Amphibole–melt trace element partitioning of fractionating calc-alkaline magmas in the lower crust: an experimental study. *Contrib. Mineral. Petrol*. **171**. s00410-016-1278-0.

Narvaez, D.F., Rose-Koga, E.F., Samaniego, P., Koga, K.T., Hidalgo, S., 2018. Constraining magma sources using primitive olivine-hosted melt inclusions from Puñalica and Sangay volcanoes (Ecuador). Contrib. Mineral. Petrol. **173**. S00410-018-1508-8.

Peccerillo, A., Taylor, S.R., 1976. Geochemistry of Eocene calc-alkaline volcanic rocks from the Kastamonu area, northern Turkey. *Contrib. Mineral. Petrol.* **58**, 63–81.

Plank, T., 2014. The chemical composition of subducting sediments. In *Treatise on Geochemistry (2nd Edition)* (eds. H.D. Holland, K.K. Turekian). Elsevier. pp. 607-629.

Price, Richard C., George, R., Gamble, J.A., Turner, S., Smith, I.E.M., Cook, C., Hobden, B., Dosseto, A., 2007. U–Th–Ra fractionation during crustal-level andesite formation at Ruapehu volcano, New Zealand. *Chem. Geol.* **244**, 437–451.

Prowatke, S., Klemme, S., 2006. Trace element partitioning between apatite and silicate melts. *Geochim. Cosmochim. Acta* **70**, 4513–4527.

Reubi, O., Bourdon, B., Dungan, M.A., Koornneef, J.M., Sellés, D., Langmuir, C.H., Aciego, S., 2011. Assimilation of the plutonic roots of the Andean arc controls variations in U-series disequilibria at Volcan Llaima, Chile. *Earth Planet. Sci. Lett.* **303**, 37–47.

Reubi, O., Sims, K.W.W., Bourdon, B., 2014. $^{238}U$–$^{230}Th$ equilibrium in arc magmas and implications for the time scales of mantle metasomatism. *Earth Planet. Sci. Lett.* **391**, 146–158.

Richter, S., Goldberg, S.A., 2003. Improved techniques for high accuracy isotope ratio measurements of nuclear materials using thermal ionization mass spectrometry. *Int. J. Mass Spectrom.* **229**, 181–197.

Ridolfi, F., Puerini, M., Renzulli, A., Menna, M., Toulkeridis, T., 2008. The magmatic feeding system of El Reventador volcano (Sub-Andean zone, Ecuador) constrained by texture, mineralogy and thermobarometry of the 2002 erupted products. *J. Volcanol. Geotherm. Res.* **176**, 94–106.

Rosenbaum, G., Sandiford, M., Caulfield, J., Garrison, J.M., 2019. A trapdoor mechanism for slab tearing and melt generation in the northern Andes. *Geology* **47**, 23–26.

Rudnick, R.L., Gao, S., 2014. Composition of the Continental Crust. In *Treatise on Geochemistry (2nd edition)* (eds. H.D. Holland, K.K. Turekian). Elsevier. pp. 1-51.

Sallarès, V., Charvis, P., 2003. Crustal thickness constraints on the geodynamic evolution of the Galápagos Volcanic Province. *Earth Planet. Sci. Lett.* **214**, 545–559.

Samaniego, P., Eissen, J.-P., Pennec, J.-L. le, Robin, C., Hall, M.L., Mothes, P., Chavrit, D., Cotten, J., 2008. Pre-eruptive physical conditions of El Reventador volcano (Ecuador) inferred from the petrology of the 2002 and 2004–05 eruptions. *J. Volcanol. Geotherm. Res.* **176**, 82–93.

Samaniego, P., Martin, H., Monzier, M., Robin, C., Fornari, M., Eissen, J.-P., Cotten, J., 2005. Temporal Evolution of Magmatism in the Northern Volcanic Zone of the Andes: The Geology and Petrology of Cayambe Volcanic Complex (Ecuador). *J. Petrol.* **46**, 2225–2252.

Schaefer, S.J., Sturchio, N.C., Murrell, M.T., Stanley, W.N., 1993. Internal 238U-series systematics of pumice from the November 13, 1985, eruption of Nevado del Ruiz, Colombia. *Geochim. Cosmochim. Acta* **57**, 1215–1219.

Schmidt, M.W., Jagoutz, O., 2017. The global systematics of primitive arc melts. *Geochem. Geophys. Geosyst.* **18**, 2817–2854.

Scott, S.R., Sims, K.W.W., Reagan, M.K., Ball, L., Schwieters, J.B., Bouman, C., Lloyd, N.S., Waters, C.L., Standish, J.J., Tollstrup, D.L., 2019. The application of abundance sensitivity filters to the precise and accurate measurement of uranium series nuclides by plasma mass spectrometry. *Int. J. Mass Spectrom.* **435**, 321–332.

Sigmarsson, O., Martin, H., Knowles, J., 1998. Melting of a subducting oceanic crust from U–Th disequilibria in austral Andean lavas. *Nature* **394**, 566–569.

Sims, Kenneth W.W., Blichert-Toft, J., Kyle, P.R., Pichat, S., Gauthier, P.J., Blusztajn, J., Kelly, P., Ball, L., Layne, G., 2008a. A Sr, Nd, Hf, and Pb isotope perspective on the genesis and long-term evolution of alkaline magmas from Erebus volcano, *Antarctica. J. Volcanol. Geotherm. Res.* **177**, 606–618.

Sims, K.W.W., DePaolo, D.J., Murrell, M.T., Baldridge, W.S., Goldstein, S., Clague, D., Jull, M., 1999. Porosity of the melting zone and variations in the solid mantle upwelling rate beneath Hawaii: inferences from $^{238}$U-$^{230}$Th-$^{226}$Ra and $^{235}$U-$^{231}$Pa disequilibria. *Geochim. Cosmochim. Acta* **63**, 4119–4138.

Sims, K.W.W., DePaolo, D.J., Murrell, M.T., Baldridge, W.S., Goldstein, S.J., Clague, D.A., 1995. Mechanisms of Magma Generation Beneath Hawaii and Mid-Ocean Ridges: Uranium/Thorium and Samarium/Neodymium Isotopic Evidence. *Science* **267**, 508-512.

Sims, K.W.W., Gill, J.B., Dosseto, A., Hoffmann, D.L., Lundstrom, C.C., Williams, R.W., Ball, L., Tollstrup, D., Turner, S., Prytulak, J., Glessner, J.J.G., Standish, J.J., Elliott, T., 2008b. An Inter-Laboratory Assessment of the Thorium Isotopic Composition of Synthetic and Rock Reference Materials. *Geostand. Geoanal. Res.* **32**, 65–91.

Sims, K.W.W., Goldstein, S.J., Blichert-toft, J., Perfit, M.R., Kelemen, P., Fornari, D.J., Michael, P., Murrell, M.T., Hart, S.R., DePaolo, D.J., Layne, G., Ball, L., Jull, M., Bender, J., 2002. Chemical and isotopic constraints on the generation and transport of magma beneath the East Pacific Rise. *Geochim. Cosmochim. Acta* **66**, 3481–3504.

Sims, K.W.W., Hart, S.R., 2006. Comparison of Th, Sr, Nd and Pb isotopes in oceanic basalts: Implications for mantle heterogeneity and magma genesis. *Earth Planet. Sci. Lett.* **245**, 743–761.

Sims, K.W.W., Hart, S.R., Reagan, M.K., Blusztajn, J., Staudigel, H., Sohn, R.A., Layne, G.D., Ball, L.A., Andrews, J., 2008c. $^{238}$U-$^{230}$Th-$^{226}$Ra-$^{210}$Pb-$^{210}$Po, $^{232}$Th-$^{228}$Ra, and $^{235}$U-$^{231}$Pa constraints on the ages and petrogenesis of Vailulu'u and Malumalu Lavas, Samoa. *Geochem., Geophys., Geosyst.* **9**, 10.1029/2007GC001651.

Sims, Kenneth W.W., Maclennan, J., Blichert-Toft, J., Mervine, E.M., Blusztajn, J., Grönvold, K., 2013a. Short length scale mantle heterogeneity beneath Iceland probed by glacial modulation of melting. *Earth Planet. Sci. Lett.* **379**, 146–157.

Sims, Kenneth W.W., Pichat, S., Reagan, M.K., Kyle, P.R., Dulaiova, H., Dunbar, N.W., Prytulak, J., Sawyer, G., Layne, G.D., Blichert-Toft, J., 2013b. On the time scales of magma genesis, melt evolution, crystal growth rates and magma degassing in the Erebus volcano magmatic system using the $^{238}$U, $^{235}$U and $^{232}$Th decay series. *J. Petrol.* **54**, 235–271.

Spiegelman, M., Elliott, T., 1993. Consequences of melt transport for uranium series disequilibrium in young lavas. *Earth Planet. Sci. Lett.* **118**, 1–20.

Spera, F.J., Bohrson, W.A., 2001. Energy-Constrained Open-System Magmatic Processes I: General Model and Energy-Constrained Assimilation and Fractional Crystallization (EC-AFC) Formulation. *J. Petrol.* **42**, 999–1018.

Stracke, A., Bourdon, B., 2009. The importance of melt extraction for tracing mantle heterogeneity. *Geochim. Cosmochim. Acta* **73**, 218–238.

Sun, S.-S., McDonough, W.F., 1989. Chemical and isotopic systematics of oceanic basalts: implications for mantle composition and processes. In *Magmatism in the Ocean Basins* (eds. A.D. Saunders, M.J. Norry). Geol. Soc., London, Special Publications 42, 313–345.

Sturm, M.E., Goldstein, S.J., Klein, E.M., Karson, J.A., Murrell, M.T., 2000. Uranium-series age constraints on lavas from the axial valley of the Mid-Atlantic Ridge, MARK area. *Earth Planet. Sci. Lett.* **181**, 61–70.

Syracuse, E.M., Abers, G.A., 2006. Global compilation of variations in slab depth beneath arc volcanoes and implications. *Geochem. Geophys. Geosyst*. **7**, 2005GC001045.

Syracuse, E.M., Van Keken, P.E., Abers, G.A., 2010. The global range of subduction zone thermal models. *Phys. Earth Planet. Inter.* **183**, 73–90.

Tepley, F.J., Lundstrom, C.C., McDonough, W.F., Thompson, A., 2010. Trace element partitioning between high-An plagioclase and basaltic to basaltic andesite melt at 1 atmosphere pressure. *Lithos* **118**, 82–94.

Tepley, F.J., Lundstrom, C.C., Sims, K.W.W., Hékinian, R., 2004. U-series disequilibria in MORB from the Garrett Transform and implications for mantle melting. *Earth Planet. Sci. Lett.* **223**, 79–97.

Thirlwall, M.F., 2002. Multicollector ICP-MS analysis of Pb isotopes using a $^{207}$Pb-$^{204}$Pb double spike demonstrates up to 400 ppm/amu systematic errors in TI-normalization. *Chem. Geol.* **184**, 255–279.

Thomas, R.B., Hirschmann, M.M., Cheng, H., Reagan, M.K., Lawrence Edwards, R., 2002. ($^{231}$Pa/$^{235}$U)-($^{230}$Th/$^{238}$U) of young mafic volcanic rocks from Nicaragua and Costa Rica and the influence of flux melting on U-series systematics of arc lavas. *Geochim. Cosmochim. Acta* **66**, 4287–4309.

Turner, S., Bourdon, B., Gill, J., 2003. Insights into Magma Genesis at Convergent Margins from U-series Isotopes. *Rev. Mineral. Geochem.* **52**, 255–315.

Turner, S., Foden, J., 2001. U, Th and Ra disequilibria, Sr, Nd and Pb isotope and trace element variations in Sunda arc lavas: predominance of a subducted sediment component. *Contrib. Mineral. Petrol.* **142**, 43–57.

Vervoort, J.D., Plank, T., Prytulak, J., 2011. The Hf–Nd isotopic composition of marine sediments. *Geochim. Cosmochim. Acta* **75**, 5903–5926.

Waters, C.L., Sims, K.W.W., Klein, E.M., White, S.M., Reagan, M.K., Girard, G., 2013. Sill to surface: Linking young off-axis volcanism with subsurface melt at the overlapping spreading center at 9º03′ N. East Pacific Rise. *Earth Planet. Sci. Lett.* **369**, 59–70.

Waters, C.L., Sims, K.W.W., Perfit, M.R., Blichert-Toft, J., Blusztajn, J., 2011. Perspective on the Genesis of E-MORB from Chemical and Isotopic Heterogeneity at 9–10°N East Pacific Rise. *J. Petrol.* **52**, 565–602.

Walker, J.A., Erik Mickelson, J., Thomas, R.B., Patino, L.C., Cameron, B., Carr, M.J., Feigenson, M.D., Lawrence E.R., 2007. U-series disequilibria in Guatemalan lavas, crustal contamination, and implications for magma genesis along the Central American subduction zone. *J. Geophys. Res. Solid Earth* **112**, 2006JB004589

Werner, R., Hoernle, K., Barckhausen, U., Hauff, F., 2003. Geodynamic evolution of the Galápagos hot spot system (Central East Pacific) over the past 20 m.y.: Constraints from morphology, geochemistry, and magnetic anomalies. *Geochem. Geophys. Geosyst.* **4**, 2003GC000576.

Williams, R.W., Gill, J.B., 1989. Effects of partial melting on the uranium decay series. *Geochim. Cosmochim. Acta* **53**, 1607–1619.

Workman, R. K., and Hart, S. R., 2005. Major and trace element composition of the depleted MORB mantle (DMM). *Earth Planet. Sci. Lett*. **231**, 53–72.

Yepes, H., Audin, L., Alvarado, A., Beauval, C., Aguilar, J., Font, Y., Cotton, F., 2016. A new view for the geodynamics of Ecuador: Implication in seismogenic source definition and seismic hazard assessment. *Tectonics* **35**, 1249–1279.

Yogodzinski, G.M., Brown, S.T., Kelemen, P.B., Vervoort, J.D., Portnyagin, M., Sims, K.W.W., Hoernle, K., Jicha, B.R., Werner, R., 2015. The Role of Subducted Basalt in the Source of Island Arc Magmas: Evidence from Seafloor Lavas of the Western Aleutians. *J. Petrol.* **56**, 441–492.

Yogodzinski, G.M., Lees, J.M., Churikova, T.G., Dorendorf, F., Wöerner, G., Volynets, O.N., 2001. Geochemical evidence for the melting of subducting oceanic lithosphere at plate edges. *Nature* **409**, 500–504.

Zou, H., Zindler, A., Niu, Y., 2002. Constraints on Melt Movement Beneath the East Pacific Rise From $^{230}$Th- $^{238}$U Disequilibrium. *Science* **295**, 107–110.

1371

Table 1 Sr, Nd, Hf, and Pb isotope data for Reventador lavas

| Sample | Eruption year | $^{87}Sr/^{86}Sr$ | 2 SE | $^{143}Nd/^{144}Nd$ | 2 SE | $\varepsilon_{Nd}$ | 2 SE | $^{176}Hf/^{177}Hf$ | 2 SE | $\varepsilon_{Hf}$ | 2 SE | $^{206}Pb/^{204}Pb$ | 2 SE | $^{207}Pb/^{204}Pb$ | 2 SE | $^{208}Pb/^{204}Pb$ | 2 SE |
|---|---|---|---|---|---|---|---|---|---|---|---|---|---|---|---|---|---|
| REV 117 | 1944 | 0.704504 | 6 | 0.512774 | 5 | 2.65 | 10 | 0.282925 | 4 | 5.42 | 15 | 18.6220 | 8 | 15.6083 | 8 | 38.5110 | 23 |
| REV 118 | 1944 | 0.704493 | 7 | 0.512776 | 6 | 2.69 | 12 | 0.282924 | 4 | 5.37 | 14 | 18.6189 | 5 | 15.6101 | 6 | 38.5115 | 19 |
| REV 125 | 1976 | 0.704589 | 7 | 0.512731 | 4 | 1.81 | 8 | 0.282908 | 7 | 4.82 | 23 | 18.5761 | 5 | 15.6068 | 6 | 38.4827 | 18 |
| REV 002 | 2002 | 0.704517 | 9 | 0.512747 | 7 | 2.13 | 14 | 0.282915 | 4 | 5.05 | 13 | 18.6042 | 8 | 15.6085 | 8 | 38.5044 | 25 |
| REV 003 | 2002 | 0.704530 | 9 | 0.512741 | 4 | 2.01 | 8 | 0.282903 | 5 | 4.62 | 17 | 18.5949 | 6 | 15.6083 | 7 | 38.4906 | 20 |
| REV 004 | 2002 | 0.704516 | 8 | 0.512749 | 5 | 2.17 | 10 | 0.282908 | 4 | 4.81 | 14 | 18.5982 | 6 | 15.6087 | 6 | 38.4980 | 17 |
| REV 005 | 2002 | 0.704511 | 11 | | | | | | | | | 18.5986 | 5 | 15.6084 | 5 | 38.4974 | 13 |
| REV 121 | 2002 | 0.704454 | 7 | 0.512768 | 5 | 2.54 | 10 | 0.282915 | 5 | 5.06 | 16 | 18.6294 | 12 | 15.6111 | 13 | 38.5202 | 36 |
| REV 126 | 2002 | 0.704492 | 9 | 0.512752 | 5 | 2.22 | 10 | 0.282922 | 5 | 5.31 | 18 | 18.6095 | 7 | 15.6111 | 7 | 38.5103 | 24 |
| REV 122 | 2005 | 0.704538 | 8 | 0.512777 | 4 | 2.72 | 8 | 0.282901 | 7 | 4.55 | 26 | 18.6003 | 5 | 15.6086 | 4 | 38.4978 | 14 |
| REV 127 | 2007 | 0.704444 | 6 | 0.512775 | 4 | 2.68 | 8 | 0.282917 | 9 | 5.13 | 32 | 18.6328 | 5 | 15.6077 | 5 | 38.5135 | 13 |
| REV 129 | 2007 | 0.704428 | 1 | 0.512782 | 5 | 2.81 | 10 | 0.282917 | 3 | 5.13 | 12 | 18.6327 | 10 | 15.6089 | 10 | 38.5159 | 30 |
| REV 001 | 2008 | 0.704489 | 8 | 0.512771 | 4 | 2.59 | 8 | 0.282919 | 4 | 5.20 | 16 | 18.6125 | 7 | 15.6066 | 8 | 38.4969 | 23 |
| REV 006 | 2008 | 0.704471 | 9 | 0.512770 | 5 | 2.57 | 10 | 0.282918 | 5 | 5.18 | 16 | 18.6124 | 8 | 15.6070 | 7 | 38.4976 | 22 |
| REV 123 | 2008 | 0.704420 | 11 | 0.512782 | 5 | 2.81 | 10 | 0.282927 | 3 | 5.46 | 12 | 18.6396 | 8 | 15.6120 | 7 | 38.5251 | 22 |
| REV 124 | 2009 | 0.704475 | 6 | 0.512760 | 5 | 2.38 | 10 | 0.282912 | 5 | 4.96 | 19 | 18.6062 | 9 | 15.6100 | 9 | 38.5026 | 28 |
| REV 200 | 2016 | 0.704553 | 9 | 0.512741 | 7 | 2.02 | 14 | 0.282887 | 4 | 4.05 | 15 | 18.5801 | 5 | 15.6068 | 5 | 38.4824 | 16 |
| REV 201 | 2016 | 0.704541 | 8 | 0.512741 | 6 | 2.01 | 12 | 0.282880 | 4 | 3.81 | 13 | 18.5848 | 4 | 15.6087 | 4 | 38.4891 | 12 |
| REV 202 | 2016 | 0.704541 | 7 | 0.512748 | 7 | 2.14 | 14 | 0.282881 | 4 | 3.87 | 14 | 18.5828 | 5 | 15.6094 | 6 | 38.4888 | 14 |
| REV 203 | 2016 | 0.704568 | 9 | 0.512724 | 6 | 1.68 | 11 | 0.282891 | 3 | 4.21 | 11 | 18.5860 | 5 | 15.6088 | 5 | 38.4882 | 14 |
| Basement Samples: | | | | | | | | | | | | | | | | | |
| REV 130 | | 0.704376 | 8 | 0.512823 | 9 | 3.60 | 18 | 0.283204 | 9 | 15.27 | 31 | 18.4561 | 4 | 15.5892 | 4 | 38.2647 | 12 |
| SU 11 | | 0.705654 | 2 | 0.512601 | 6 | -0.73 | 12 | 0.282792 | 4 | 0.72 | 15 | 18.0431 | 5 | 15.5777 | 6 | 37.8712 | 14 |
| SU 112 | | | | 0.512691 | 2 | 1.03 | 5 | 0.282834 | 2 | 2.19 | 13 | | | | | | |
| Quality Assurance Standards: | | | | | | | | | | | | | | | | | |

| | | | | | | | | | | | | | | | | |
|---|---|---|---|---|---|---|---|---|---|---|---|---|---|---|---|---|
| AGV-2 | 0.703979 (2) | 3 | 0.512783 (1) | 8 | 2.82 | 0.15 | 0.282971 (1) | 3 | 7.00 | 0.09 | 18.8656 (4) | 68 | 15.6203 (4) | 11 | 38.539 (4) | 75 |
| BCR-1 | 0.704996 (1) | 8 | 0.512640 (9) | 5 | 0.04 | 0.13 | 0.282862 (1) | 4 | 3.19 | 0.13 | 18.8207 (1) | 6 | 15.6371 (1) | 5 | 38.7263 (1) | 14 |

Notes: Errors reported as 2 standard error, and expressed as uncertainty in the last decimal place(s).

Nd isotopes are normalized to a chondritic value of $^{143}Nd/^{144}Nd = 0.512638$. Hf isotopes are normalized to a chondritic value of $^{176}Hf/^{177}Hf = 0.282772$.

For quality assurance standards AGV-2 and BCR-1, numbers in parentheses indicate number of measurements conducted during the course of this study. Uncertainties are 2 SE.

AGV-2 (mean ± 2σ): $^{87}Sr/^{86}Sr = 0.703981\pm0.000009$, $^{143}Nd/^{144}Nd = 0.512791\pm0.000013$, $^{176}Hf/^{177}Hf = 0.282984\pm0.000009$, $^{206}Pb/^{204}Pb = 18.8688\pm.0063$, $^{207}Pb/^{204}Pb = 15.6173\pm0.0071$, $^{208}Pb/^{204}Pb = 38.5443\pm0.0135$ (Weis et al., 2006; 2007).

BCR-1 (mean ± 2σ): $^{87}Sr/^{86}Sr = 0.705018\pm0.000013$, $^{143}Nd/^{144}Nd = 0.512638\pm0.000006$, $^{176}Hf/^{177}Hf = 0.282875\pm0.000003$, $^{206}Pb/^{204}Pb = 18.8225\pm.00031$, $^{207}Pb/^{204}Pb = 15.6363\pm0.0033$, $^{208}Pb/^{204}Pb = 38.7321\pm0.0073$ (Weis et al., 2006; 2007).

GEOREM Recommended values for AGV-2 (mean ± 2σ): $^{87}Sr/^{86}Sr = 0.704035\pm0.0000155$, $^{143}Nd/^{144}Nd = 0.51278\pm0.00022$, $^{176}Hf/^{177}Hf = 0.282978\pm0.000011$, $^{206}Pb/^{204}Pb = 18.939\pm.005$, $^{207}Pb/^{204}Pb = 15.654\pm0.003$, $^{208}Pb/^{204}Pb = 38.56\pm0.006$

GEOREM recommended values BCR-1 (mean ± 2σ): $^{87}Sr/^{86}Sr = 0.705014\pm0.0000033$, $^{143}Nd/^{144}Nd = 0.512615\pm0.000121$, $^{176}Hf/^{177}Hf = 0.282867\pm0.000015$, $^{206}Pb/^{204}Pb = 18.813\pm.009$, $^{207}Pb/^{204}Pb = 15.632\pm0.006$, $^{208}Pb/^{204}Pb = 38.727\pm0.032$

1372

Table 2: U-Series data for El Reventador lavas

| Sample | Eruption Year | U (ppm) | 2$\sigma$ | Th (ppm) | 2$\sigma$ | ($^{238}$U/$^{232}$Th) | 2$\sigma$ | ($^{230}$Th/$^{232}$Th) | 2 SE | ($^{230}$Th/$^{238}$U) | 2 SE | ($^{234}$U/$^{238}$U) | 2 SE |
|---|---|---|---|---|---|---|---|---|---|---|---|---|---|
| REV 117 | 1944 | 1.00 | 0.02 | 4.19 | 0.05 | 0.971 | 0.018 | 1.048 | 0.010 | 1.080 | 0.023 | 1.001 | 0.002 |
| REV 118 | 1944 | 1.81 | 0.02 | 5.25 | 0.06 | 1.047 | 0.019 | 1.062 | 0.011 | 1.014 | 0.021 | 1.000 | 0.004 |
| REV 125 | 1976 | 1.76 | 0.02 | 5.26 | 0.06 | 1.014 | 0.019 | 0.984 | 0.010 | 0.970 | 0.020 | 1.001 | 0.003 |
| REV 001 | 2008 | 1.46 | 0.02 | 4.42 | 0.06 | 1.001 | 0.018 | 1.042 | 0.010 | 1.041 | 0.022 | 1.001 | 0.002 |
| REV 002 | 2002 | 1.29 | 0.02 | 3.96 | 0.05 | 0.985 | 0.018 | 1.029 | 0.010 | 1.044 | 0.022 | 1.000 | 0.004 |
| REV 003 | 2002 | 1.28 | 0.02 | 4.11 | 0.05 | 0.944 | 0.017 | 1.028 | 0.010 | 1.089 | 0.023 | 1.001 | 0.003 |
| REV 004 | 2002 | 2.03 | 0.03 | 5.52 | 0.07 | 1.115 | 0.021 | 1.003 | 0.010 | 0.900 | 0.019 | 1.000 | 0.002 |
| REV 005 | 2002 | 2.21 | 0.03 | 5.67 | 0.07 | 1.181 | 0.022 | 1.024 | 0.011 | 0.867 | 0.019 | 1.002 | 0.001 |
| REV 121 | 2002 | 1.38 | 0.02 | 4.06 | 0.05 | 1.029 | 0.019 | 1.119 | 0.014 | 1.088 | 0.024 | 1.002 | 0.003 |
| REV 126 | 2002 | 1.90 | 0.03 | 5.30 | 0.06 | 1.091 | 0.020 | 1.036 | 0.010 | 0.949 | 0.020 | 1.002 | 0.003 |
| REV 122 | 2005 | 1.33 | 0.02 | 4.11 | 0.05 | 0.982 | 0.018 | 1.043 | 0.011 | 1.063 | 0.019 | 1.003 | 0.001 |
| REV 127 | 2007 | 1.49 | 0.02 | 4.70 | 0.06 | 0.965 | 0.018 | 1.025 | 0.011 | 1.063 | 0.019 | 1.002 | 0.001 |
| REV 129 | 2007 | 1.53 | 0.02 | 4.70 | 0.06 | 0.989 | 0.018 | 1.065 | 0.011 | 1.076 | 0.023 | 1.002 | 0.002 |
| REV 006 | 2008 | 1.45 | 0.02 | 4.40 | 0.05 | 1.001 | 0.018 | 1.031 | 0.010 | 1.030 | 0.022 | 1.001 | 0.002 |
| REV 123 | 2008 | 1.59 | 0.02 | 4.66 | 0.06 | 1.035 | 0.019 | 1.048 | 0.011 | 1.012 | 0.021 | 1.001 | 0.002 |
| REV 124 | 2009 | 1.51 | 0.02 | 4.59 | 0.06 | 0.997 | 0.018 | 1.071 | 0.011 | 1.074 | 0.022 | 1.003 | 0.004 |
| REV 200 | 2016 | 1.66 | 0.02 | 5.19 | 0.06 | 0.968 | 0.018 | 0.983 | 0.010 | 1.015 | 0.019 | 1.004 | 0.001 |
| REV 201 | 2016 | 1.58 | 0.02 | 4.94 | 0.06 | 0.972 | 0.018 | 0.998 | 0.010 | 1.026 | 0.019 | 1.002 | 0.001 |
| REV 202 | 2016 | 1.58 | 0.02 | 5.08 | 0.06 | 0.944 | 0.017 | 0.979 | 0.011 | 1.037 | 0.019 | 1.002 | 0.002 |
| REV 203 | 2016 | 1.66 | 0.02 | 5.07 | 0.06 | 0.995 | 0.018 | 0.983 | 0.010 | 0.988 | 0.019 | 1.002 | 0.001 |
| Basement Samples: | | | | | | | | | | | | | |
| REV 130 | | 0.83 | | 1.91 | | 1.321 | | | | | | | |
| SU 11 | | 2.08 | | 7.85 | | 0.806 | | | | | | | |
| SU 112 | | 2.63 | | 13.27 | | 0.603 | | | | | | | |
| Quality Assurance Standards: | | | | | | | | | | | | | |
| BCR-1 | | 1.70 | 0.02 | 5.87 | 0.07 | 0.878 | 0.017 | 0.882 | 0.010 | 1.004 | 0.022 | 1.004 | 0.001 |
| RGM-2 | | 5.48 | 0.08 | 14.36 | 0.18 | 1.158 | 0.220 | 1.218 | 0.010 | 1.052 | 0.022 | 1.004 | 0.001 |

Notes: activity ratios (denoted by parentheses) were calculated using the following decay constants: $\lambda_{238}$ = 1.5513x10$^{-10}$ yr$^{-1}$, $\lambda_{234}$ = 2.8263 x10$^{-6}$ yr$^{-1}$, $\lambda_{232}$ = 4.9475x 10$^{-11}$ yr$^{-1}$, $\lambda_{230}$ = 9.1577x10$^{-6}$ yr$^{-1}$

Errors ( 2$\sigma$ or 2 SE) were propagated following standard techniques and include: uncertainty in $^{233}$U and $^{229}$Th spikes used for isotope dilution and measurement precision for bracketing standards and samples

Recommended values for BCR-2 (mean ± 2$\sigma$): U = 1.665±0.051, Th = 5.762±0.275, ($^{238}$U/$^{232}$Th) = 0.883±0.31, ($^{230}$Th/$^{232}$Th) = 0.881±0.013, ($^{230}$Th/$^{238}$U) = 0.998±0.0380 (Scott et al., 2019)

1373

Table 3: Model endmember compositions

| Isotopic Compositions | $^{87}Sr/^{86}Sr$ | $\varepsilon_{Nd}$ | $\varepsilon_{Hf}$ | $^{208}Pb/^{206}Pb$ | $(^{230}Th/^{232}Th)$ | | |
|---|---|---|---|---|---|---|---|
| Parental basalt | 0.7041 | 5.5 | 9.74 | 2.053 | 1.20 | | |
| Crustal Assimilant | 0.7200 | -12 | -17.4 | 2.0989 | 0.706 | | |
| | | | | | | | |
| Concentration (ppm) | Sr | Nd | Hf | Pb | Th | La/Yb | La/Sm |
| Crustal Assimilant, Ca (Rudnick and Gao, 2014) | 320 | 20 | 3.7 | 11 | 1.2 | 10.5 | 5.13 |
| | | | | | | | |
| Parental Magma, Co (values in parentheses define shaded regions in Figures 6, 8 , and 10) | 1300 (1250 - 1350) | 8.25 (7.5 - 10) | 1.5 (1.25 - 1.75) | 1.8 (1.6-2.0) | 0.32 (0.25-0.5) | Models A-C: 19 (18-20)<br>Model D: 15<br>Model E: 13 (11.5-14.5) | 4.75 (4.5-5) |

1374

| Table 1.4: Partition Coefficients | | | | | | | | | |
|---|---|---|---|---|---|---|---|---|---|
| Partition Coefficients for individual phases[3] | Sr | Nd | Hf | Pb | U | Th | La | Sm | Yb |
| Olivine (ol) | 0.00019 | 0.001 | 0.01 | 0.0001 | 0.0001 | 0.001 | 0.0004 | 0.0013 | 0.0015 |
| Clinopyroxene (cpx) | 0.157 | 0.28 | 0.21 | 0.0102 | 0.0127 | 0.013 | 0.052 | 0.44 | 0.64 |
| Orthopyroxene (opx) | 0.0034 | 0.013 | 0.01 | 0.0013 | 0.00001 | 0.00001 | 0.0019 | 0.063 | 0.39 |
| Plagioclase (plg)[4] | 2.1 | 0.133 | 0.0038 | 0.1 | 0.01 | 0.01 | 0.205 | 0.144 | 0.0423 |
| Amphibole (amp) | 0.42 | 0.94 | 0.705 | 0.07 | 0.013 | 0.017 | 0.173 | 1.628 | 2.191 |
| Garnet (grt) | 0.0099 | 0.222 | 0.26 | 0.00012 | 0.0058 | 0.00137 | 0.024 | 0.53 | 24 |
| | | | | | | | | | |
| Model Partition Coefficients | | | | | | | | | |
| A and E (47.5% ol, 18.8% cpx, 9.4% opx, 18.8% plag, 4.5% amp, 1% gt) | 0.444 | 0.150 | 0.120 | 0.024 | 0.005 | 0.006 | 0.066 | 0.253 | 0.553 |
| B (41.7% ol, 16.5% cpx, 8.2% opx, 28.8% plag, 3.9% amp, 0.9% gt) | 0.648 | 0.148 | 0.105 | 0.033 | 0.006 | 0.006 | 0.083 | 0.240 | 0.490 |
| C (53.3% ol, 21.1% cpx, 10.6% opx, 8.8% plag, 5.1% amp, 1.1% gt) | 0.240 | 0.152 | 0.134 | 0.015 | 0.004 | 0.005 | 0.048 | 0.267 | 0.616 |
| D (47% ol, 18.6% cpx, 9.3% opx, 18.6% plag, 4.5% amp, 2% gt) | 0.439 | 0.151 | 0.121 | 0.024 | 0.005 | 0.006 | 0.065 | 0.256 | 0.790 |

[3] Binderman and Davis, 2000; Dostal et al., 1983; Dunn and Sen, 1994; Huari et al., 1994; Klein et al., 2000; Mckenzie and O'Nions, 1991; Nandedkar et al., 2016; Prowatke and Klemme, 2006)

[1]Hf partition coefficient calculated based on the Zr coefficient of Binderman and Davis, 2000; Yb partition coefficient calculated based on the Y coefficient of Binderman and Davis, 2000.

1375

**Figure Captions**

**Figure 1. A)** Map showing Reventador in relation to other volcanoes in the NVZ and important tectonic features such as the Carnegie Ridge, Grijalva Fracture Zone (GFZ), and Chingual-Cosanga-Pallatanga-Puna (CCPP) Shear Zone. Although Reventador is located between the Eastern Cordillera in the main arc and the back-arc, we classify it as a main-arc volcano (see Results). **B)** Sample locations. Also shown are the Coca River, and the EC 45, one of the main roads connecting Quito and the Inter-Andean Valley to the Amazon Basin.

**Figure 2.** Major-element composition of Reventador samples compared with NVZ main-arc and back-arc volcanics. **A)** Wt. % FeO/MgO vs. wt. % $SiO_2$ after Miyashiro, 1974. Reventador samples plot near the tholeiitic/calc-alkaline dividing line, while main-arc volcanics are generally calc-alkaline and alkaline back-arc lavas are characterized by higher FeO/MgO. **B)** Wt. % $SiO_2$ vs. wt. % $K_2O$ after Peccerillo and Taylor, 1976. Reventador samples plot near the medium-high $K_2O$ divide. Main-arc samples have low-medium $K_2O$, while back-arc samples have high $K_2O$ (For NVZ data and sources, see supplementary data – Table S2).

**Figure 3.** Trace-element compositions of Reventador samples compared with NVZ main-arc volcanics with wt. % $SiO_2 < 64$ and back-arc volcanics. **A)** Primitive mantle-normalized trace-element concentrations and **B)** chondrite-normalized REE concentrations of Reventador samples (Sun and McDonough, 1989; McDonough and Sun, 1995). Reventador samples have traits that typify arc lavas, such as LILE enrichment and HFSE

depletion. In A and B the main-arc field (gray) is the mean value of main-arc volcanics +/- 1 SD (Supplementary data – Table S2). Trace-element concentrations in Reventador samples are relatively high compared to main arc values, but much lower than Sumaco values, which represent back-arc values (Garrison et al., 2018).

**Figure 4. A)** La/Yb vs. Yb. NVZ volcanoes, including Reventador, produce lavas with high La/Yb, similar to Western Aleutian values, outlined field labeled WA. In contrast, "typical" arc lavas, such as lavas from the Marianas, outlined field labeled M, have lower La/Yb and higher Yb concentrations (Elliot et al., 1997; Yogodzinski et al., 2015, and references therein). **B)** La/Yb vs wt. % $SiO_2$. **C)** La/Sm vs. wt. % $SiO_2$.

**Figure 5.** Sr, Nd, Hf, and Pb isotope ratios of Reventador lavas, other NVZ volcanics, and potential magma sources, and model endmembers (Hammersley et al., 2022; Harpp and White, 2001; 2005; Werner et al., 2003; Workman and Hart, 2005; Jackson and Dasgupta, 2008). **A)** $\varepsilon_{Nd}$ vs $^{87}Sr/^{86}Sr$. **B)** $^{208}Pb/^{204}Pb$ vs $^{206}Pb/^{204}Pb$. **C)** $^{207}Pb/^{204}Pb$ vs $^{206}Pb/^{204}Pb$. **D)** $\varepsilon_{Nd}$ vs $\varepsilon_{Hf}$ (regional data and sources are available in Supplementary data – Table S2).

**Figure 6.** Sr, Nd, Hf, and Pb isotope ratios of Reventador lavas with AFC model results. **A)** $\varepsilon_{Nd}$ vs $^{87}Sr/^{86}Sr$. **B)** $^{208}Pb/^{206}Pb$ vs $\varepsilon_{Nd}$. **C)** $^{208}Pb/^{206}Pb$ vs $^{87}Sr/^{86}Sr$. **D)** $\varepsilon_{Hf}$ vs $\varepsilon_{Nd}$. Numbers indicate the percent crustal assimilant in the magma. A maximum of 20% assimilation is required to reproduce the observed data. The gray field shows models with $C_a/C_o$ values that bracket the data (Table 3). Models are described in section 5.4.4 and Tables 3 and 4.

**Figure 7. A, B, C, D)** $^{87}Sr/^{86}Sr$, $\varepsilon_{Nd}$, $\varepsilon_{Hf}$, and $^{208}Pb/^{206}Pb$ vs wt. % $SiO_2$.

**Figure 8.** $^{87}Sr/^{86}Sr$, $\varepsilon_{Nd}$, $\varepsilon_{Hf}$, and $^{208}Pb/^{206}Pb$ vs La/Yb **(A, B, C, D)** and La/Sm with AFC models. A maximum of 20% assimilation accompanied by fractional crystallization of a gabbroic assemblage containing olivine, plagioclase, orhopyroxene, clinopyroxene, amphibole and garnet is required to reproduce the observed data. The models are discussed in Section 5.4.5 and parameter values are listed in Tables 3 and 4.

**Figure 9.** ($^{238}U/^{232}Th$) vs ($^{230}Th/^{232}Th$) showing data from Reventador along with regional data from Cotopaxi and Nevado de Ruiz (Garrison et al., 2006; Schaffer et al., 1993) and global arc, MORB and OIB data. Dashed lines show percentages of $^{230}Th$- and $^{238}U$-excesses (Arc data is from Reubi et al., 2014 and References therein. MORB and OIB data from Bourdon et al., 1996; 2005; Goldstein et al., 1989; 1992; 1993; Lundstrom et al., 1999; Peate et al., 2001; Sims et al., 1995; 1999; 2001; 2002; 2008c; 2013b Sturm et al., 2000; Tepley et al., 2004; Zou et al., 2002)

**Figure 10 A, B, C, D, E, F)** ($^{230}Th/^{232}Th$) vs $^{87}Sr/^{86}Sr$, $\varepsilon_{Nd}$, $\varepsilon_{Hf}$, $^{208}Pb/^{206}Pb$, wt. % $SiO_2$, La/Yb, and La/Sm showing Reventador lavas and AFC model results. Numbers indicate the percent crustal assimilant in the magma. A maximum of 20% assimilation is required to reproduce the observed data. Model details are discussed in section 5.4.6 and Tables 3 and 4.

**Figure 11**. ($^{230}Th/^{238}U$) vs. **A)** wt. % $SiO_2$, **B)** La/Sm, and **C)** Pb/Ce. The dashed line shows ($^{230}Th/^{238}U$) = 1.

**Figure 12.** ($^{238}U/^{232}Th$) vs ($^{230}Th/^{232}Th$) showing data from Reventador along with model results. Metasomatism models show the effects of 5 – 10% partial melting of average EGSC basalt (Kokfeldt et al., 2005) and addition of 0.25 – 1% of these melts to the depleted mantle. Numbers on the EGSC melt model indicate the percentage partial melting of the EGSC, while numbers on the depleted mantle + EGSC melt models indicate the percentage of melt added to the depleted mantle. AFC models with $(^{230}Th/^{232}Th)_o = 1.20$, $(^{230}Th/^{232}Th)_a = 0.706$, $(^{230}Th/^{238}U)_o = 1.05 – 0.80$, and $(^{230}Th/^{238}U)_a = 1.1 – 1.3$ are also shown. AFC models are described in section 5.4.6 and Tables 3 and 4.

**Figure 13.** A comparison of FD-AFC and EC-AFC results. Endmember compositions and partition coefficients for crystallization used in both models are given in Tables 3 and 4. **A)** $\varepsilon_{Nd}$ vs $^{87}Sr/^{86}Sr$. **B)** $^{208}Pb/^{206}Pb$ vs $\varepsilon_{Nd}$. **C)** $^{208}Pb/^{206}Pb$ vs $^{87}Sr/^{86}Sr$. **D)** $\varepsilon_{Hf}$ vs $\varepsilon_{Nd}$ (Both the FD-AFC and EC-AFC models are plotted in D. However since $Nd_o/Nd_a$ and $Hf_o/Hf_a$ both equal 0.41, the model trajectories are nearly identical. For further details see section 5.4.7 of the text). For the EC-AFC model, $T_{eq}$ = 1228°C, and the other thermal parameters were set according to the standard lower crustal values given in Bohrson and Spera, 2001 (Initial magma temperature = 1320°C, initial assimilant temperature = 600°C, magma liquidus = 1320°C, assimilant liquidus = 1100°C, assimilant solidus = 900°C, specific heat of the magma = 1484 J/(kg·K), specific heat assimilant = 1388 J/(kg·K), enthalpy of fusion = 369000 J/kg, and enthalpy of crystallization = 354000 J/kg). Additionally, in the EC-AFC

model the partition coefficients for assimilation were set to one to facilitate comparison with the FD-AFC results. While the FD-AFC model reproduces the observed trends with 10-20% assimilation, the EC-AFC model requires less assimilation, 8-12% (for both models we show the percent of assimilant currently in the magma, while the EC-AFC output shows mass assimilant normalized to the initial mass magma; these numbers differ by up to 1%).

Figure 1



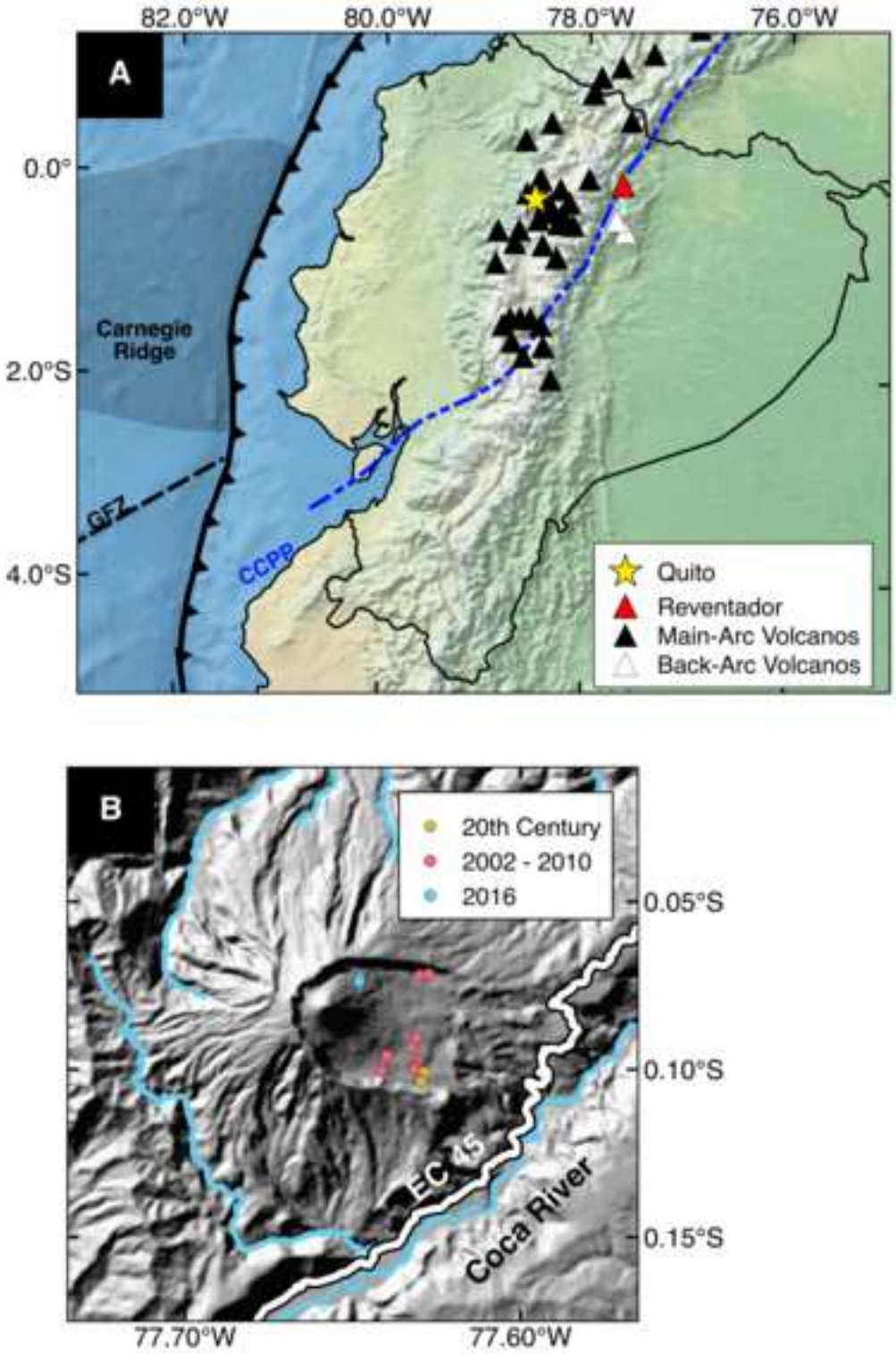

Figure 2



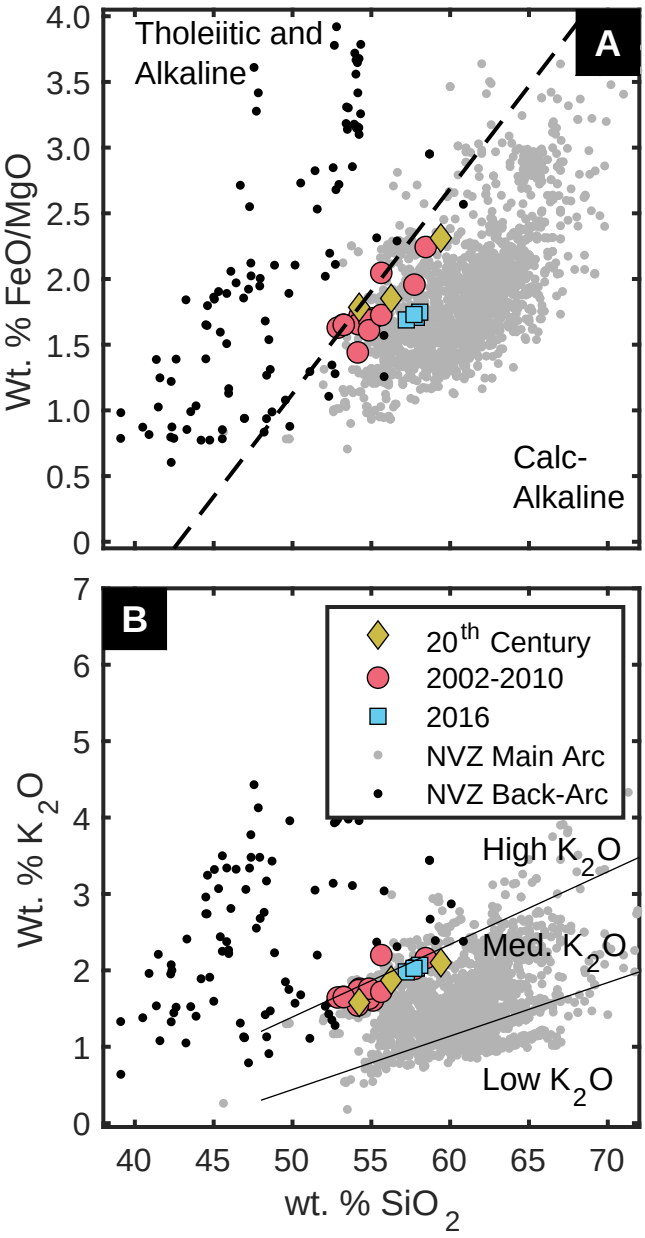

Figure 3



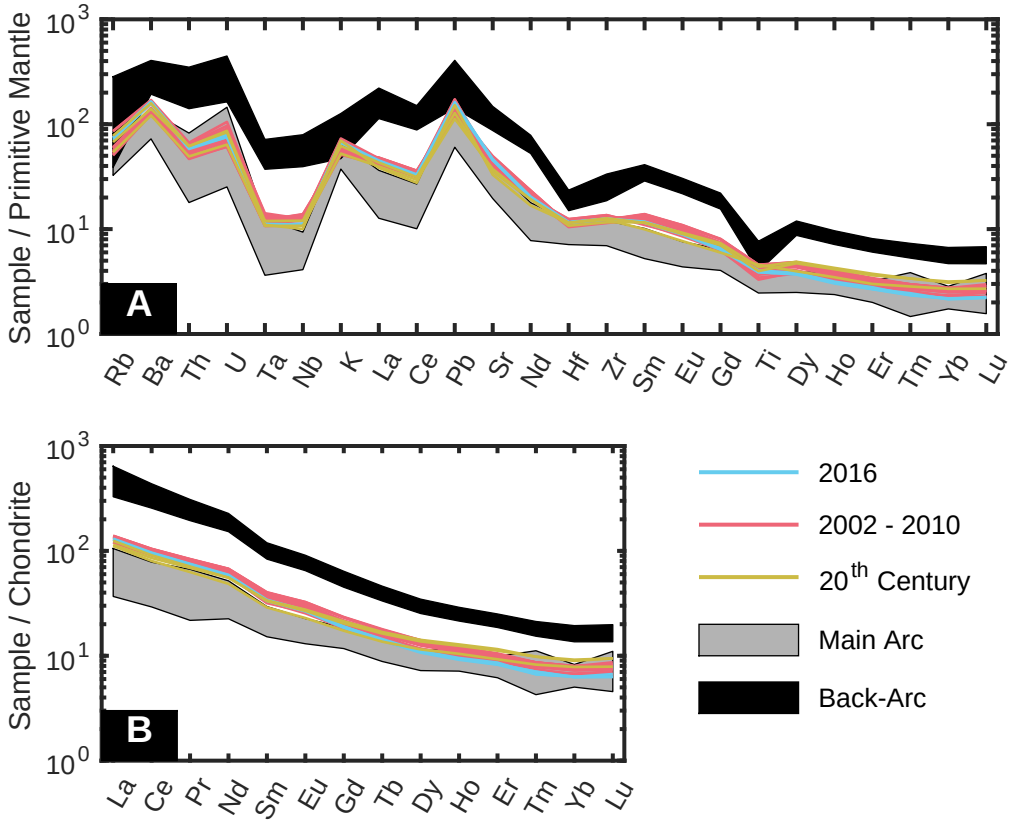

Figure 4



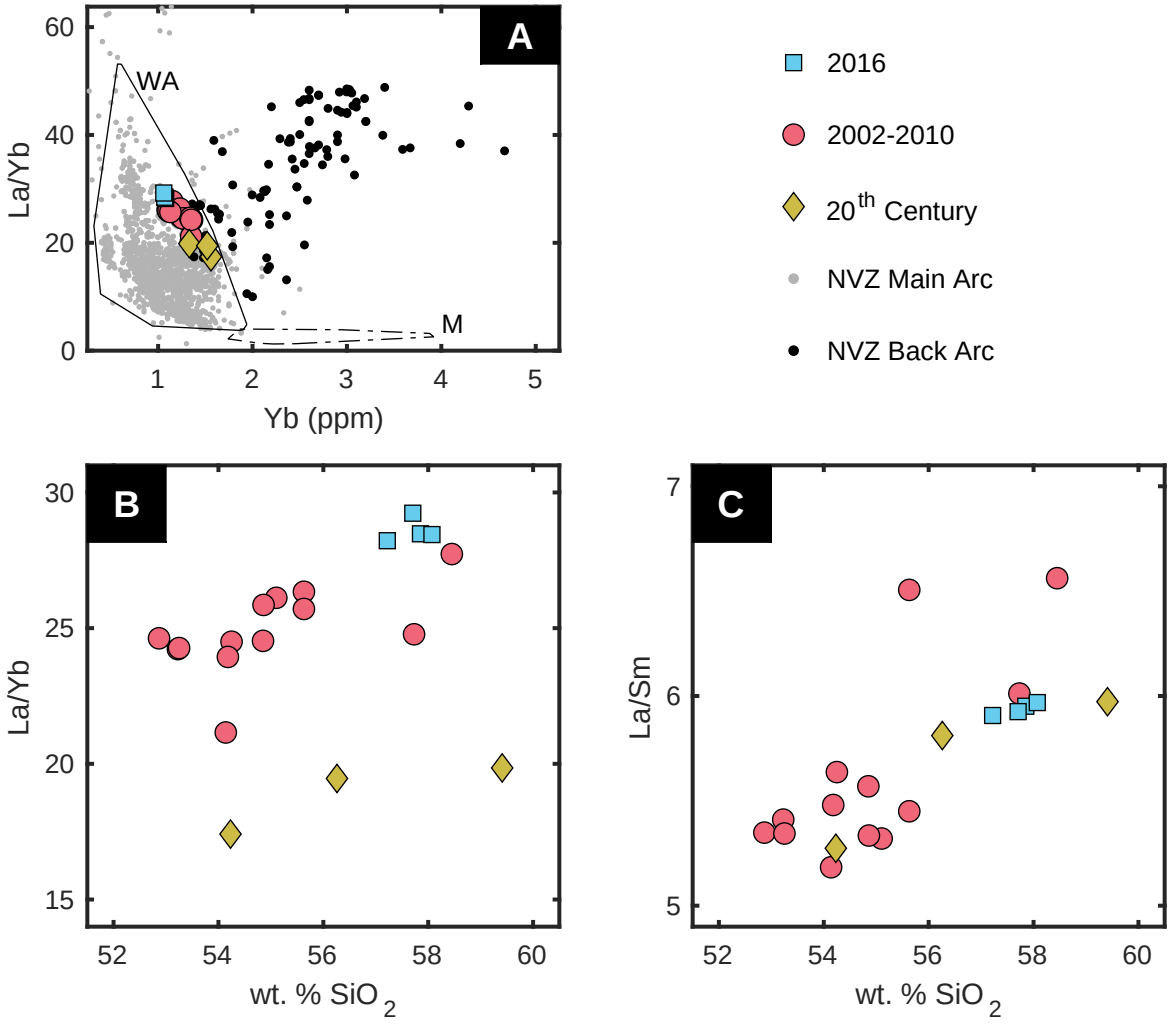

Figure 5



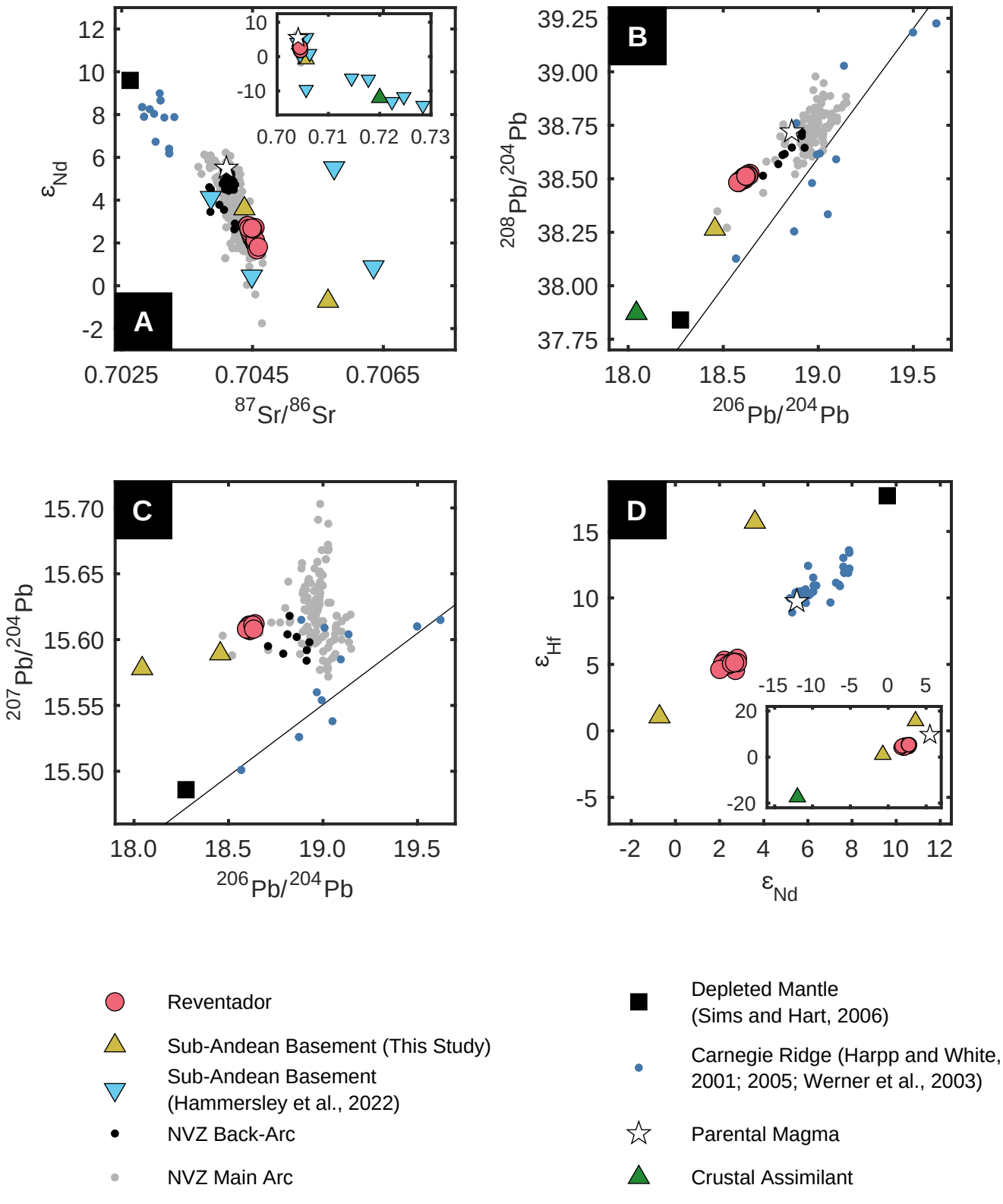

Figure 6



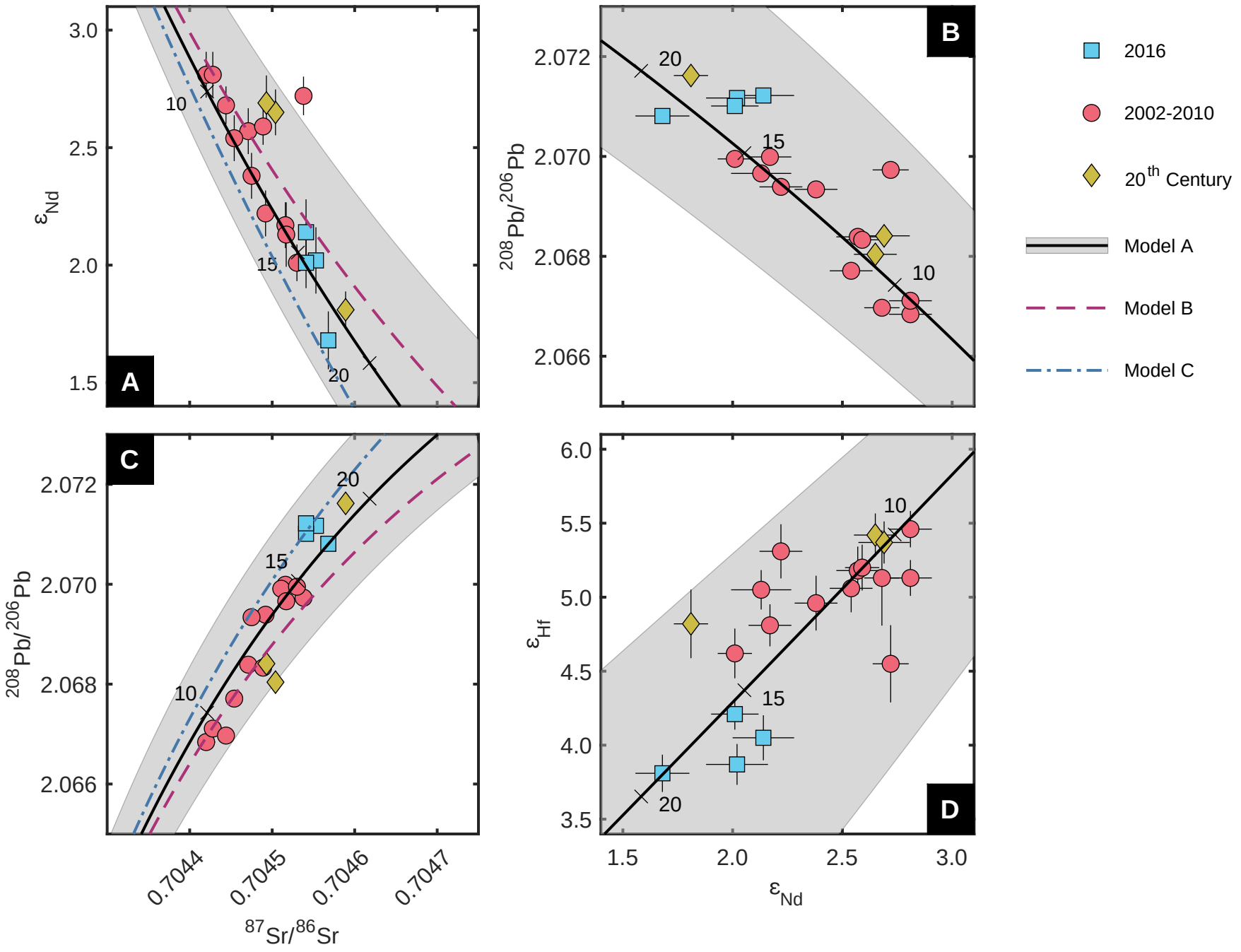

Figure 7



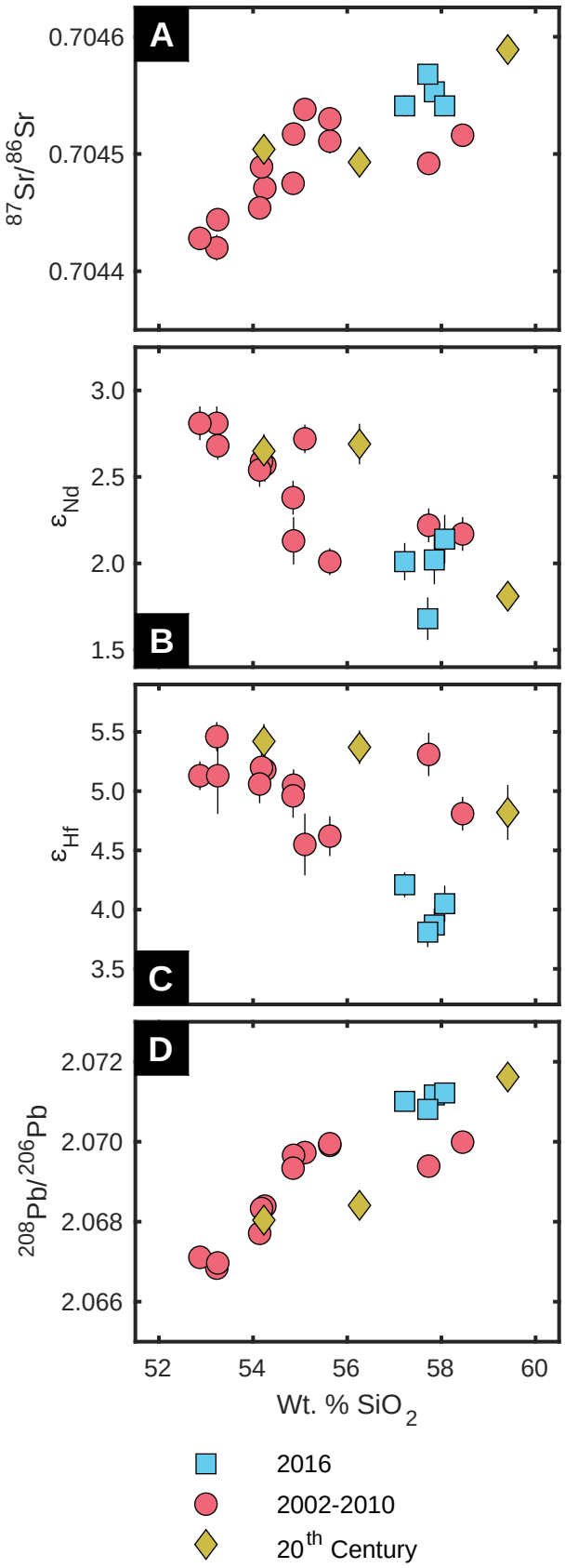

Figure 8



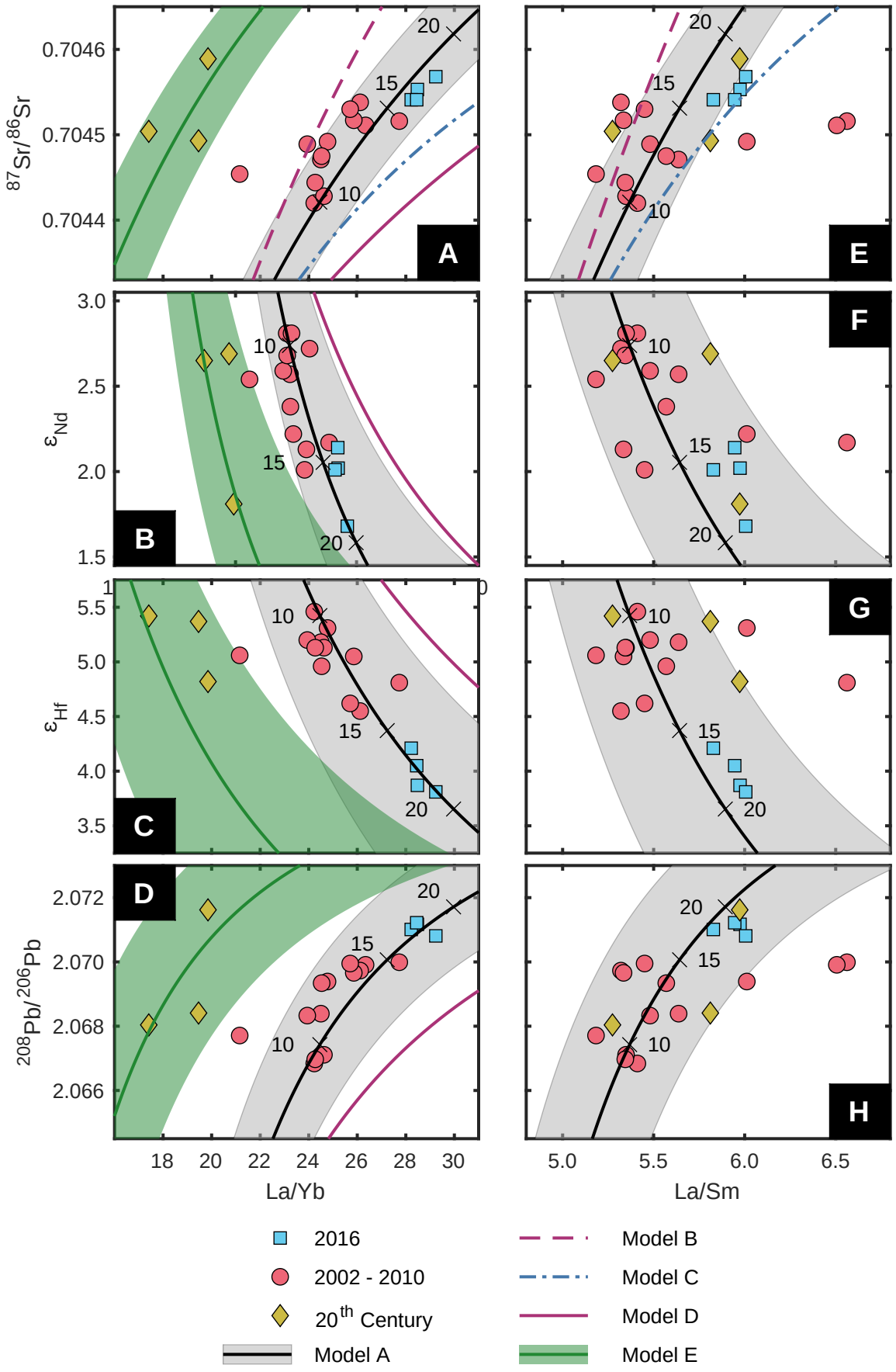

Figure 9

Click here to access/download;Figure;Figure_9_5_23.pdf

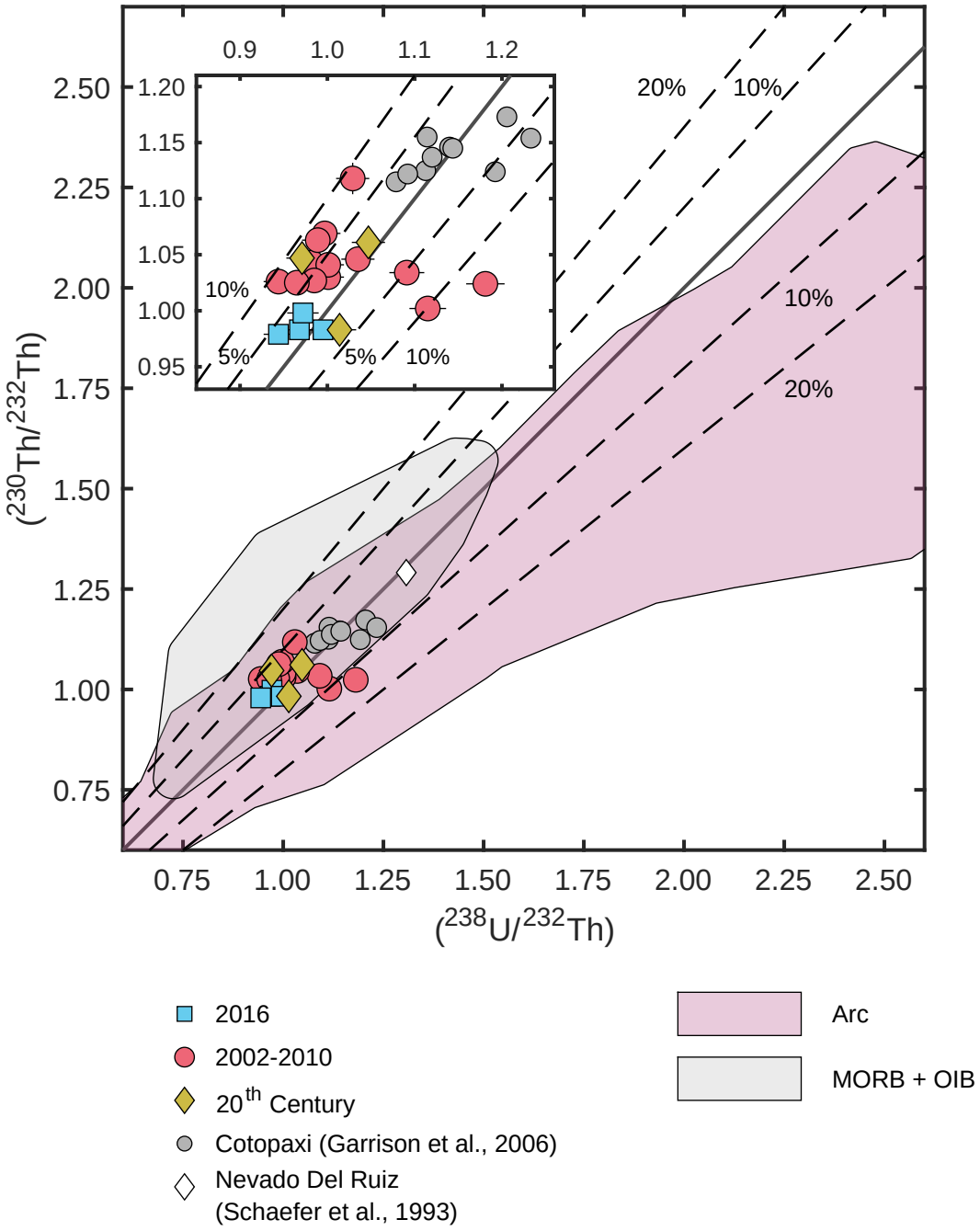

Figure 10

Click here to access/download;Figure;Figure_10.pdf

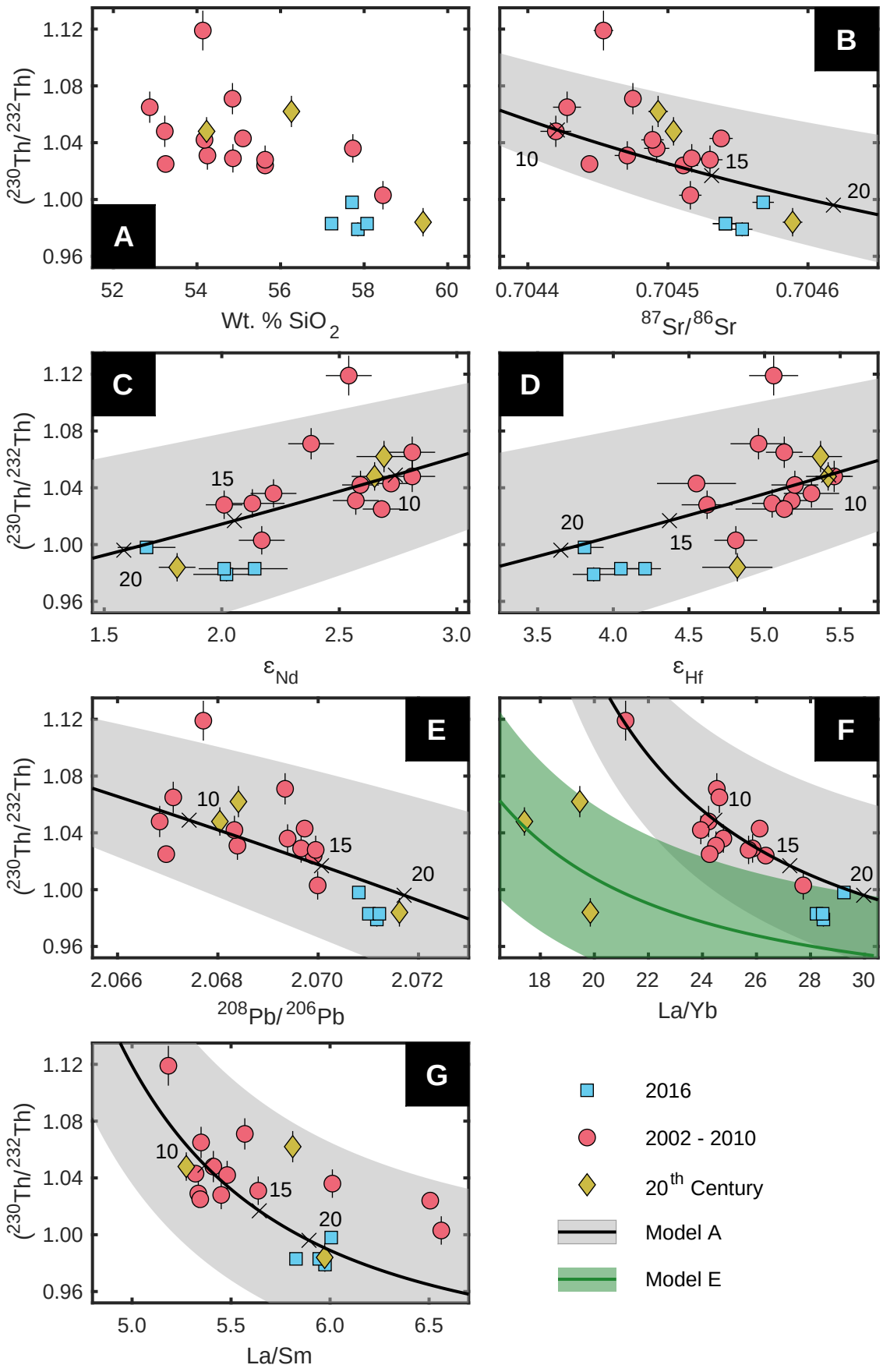

Figure 11



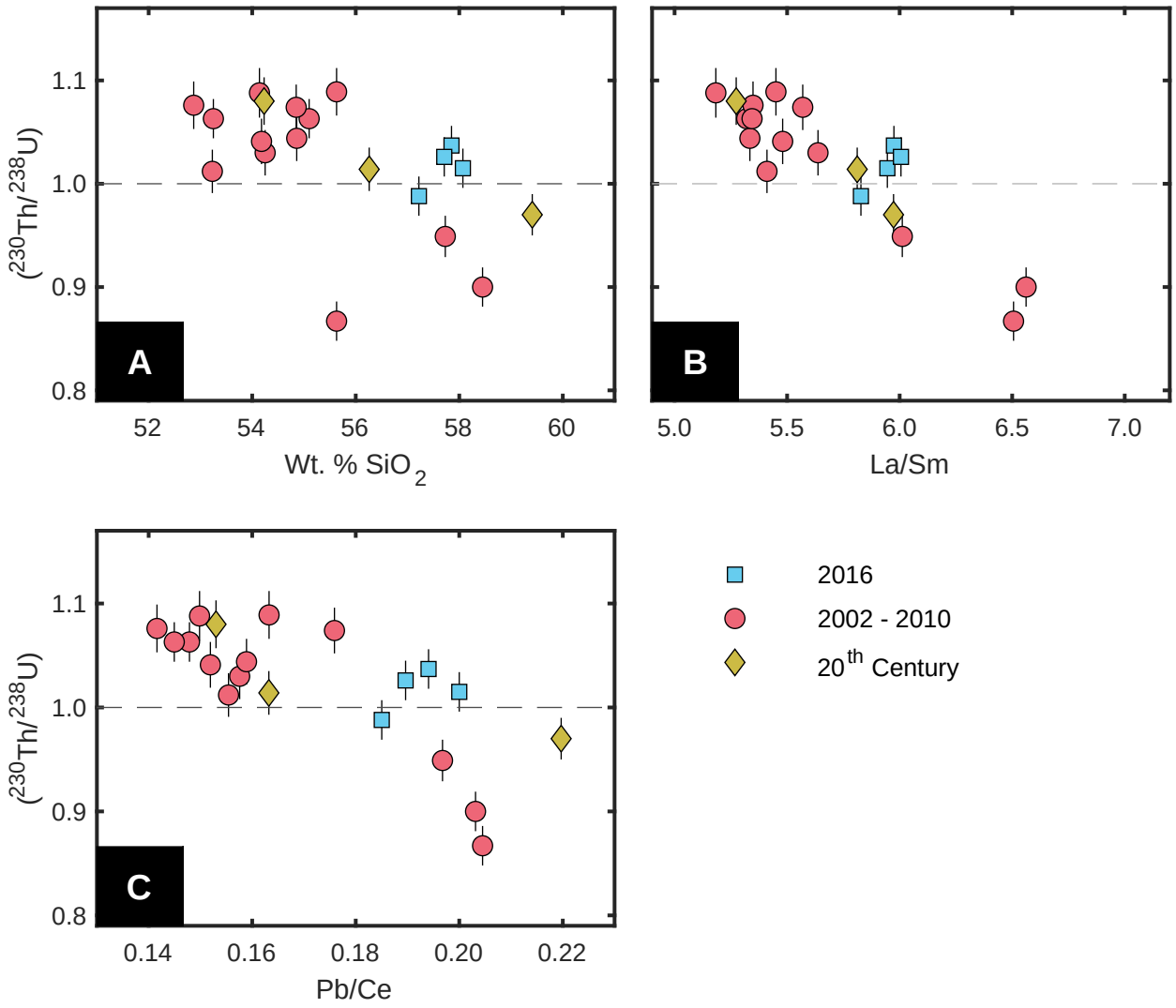

Figure 12



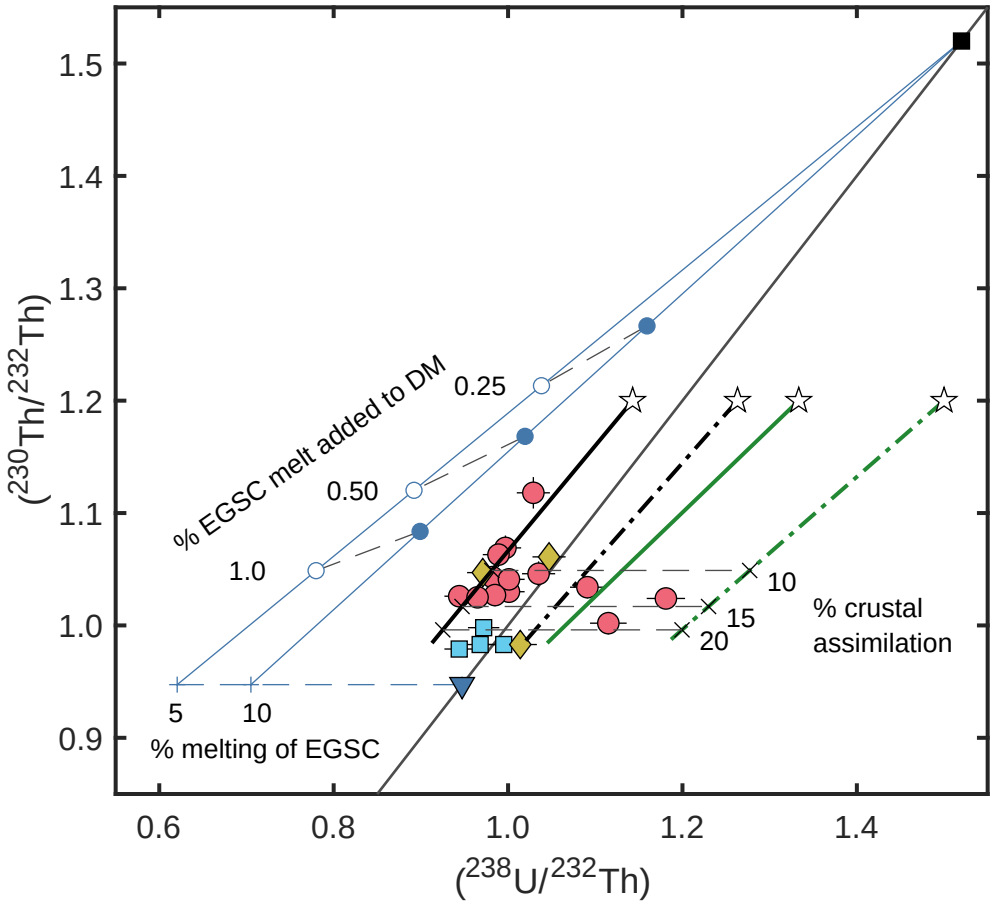


2016
2002-2010
20th Century
EGSC
Depleted mantle
Parental basalts

EGSC melt
Depleted mantle + EGSC melt (F = 10%)
Depleted mantle + EGSC melt (F = 5%)
$(^{230}Th/^{238}U)_o$ = 1.05, $(^{230}Th/^{238}U)_a$ = 1.3
$(^{230}Th/^{238}U)_o$ = 0.95, $(^{230}Th/^{238}U)_a$ = 1.1
$(^{230}Th/^{238}U)_o$ = 0.90, $(^{230}Th/^{238}U)_a$ = 1.3
$(^{230}Th/^{238}U)_o$ = 0.80, $(^{230}Th/^{238}U)_a$ = 1.1

Figure 13